

1 LEVERAGING MULTI-MESSENGER ASTROPHYSICS FOR DARK MATTER SEARCHES

By

Daniel Nicholas Salazar-Gallegos

A DISSERTATION

Submitted to
Michigan State University
in partial fulfillment of the requirements
for the degree of

Physics—Doctor of Philosophy
Computational Mathematics in Science and Engineering—Dual Major

Today

ABSTRACT

3 I did Dark Matter with HAWC and IceCube. I also used Graph Neural Networks

⁴ Copyright by

⁵ DANIEL NICHOLAS SALAZAR-GALLEGOS

⁶ Today

ACKNOWLEDGMENTS

8 I love my friends. Thanks to everyone that helped me figure this out. Amazing thanks to the people
9 at LANL who supported me. Eames, etc Dinner Parties Jenny and her child Kaydince Kirsten, Pat,
10 Andrea Family. You're so far but so critical to my formation. Unconditional love. Roommate

TABLE OF CONTENTS

12	LIST OF TABLES	vii
13	LIST OF FIGURES	viii
14	LIST OF ABBREVIATIONS	xii
15	CHAPTER 1 INTRODUCTION	1
16	CHAPTER 2 DARK MATTER IN THE COSMOS	2
17	2.1 Introduction	2
18	2.2 Dark Matter Basics	3
19	2.3 Evidence for Dark Matter	4
20	2.4 Searching for Dark Matter: Particle DM	11
21	2.5 Sources for Indirect Dark Matter Searches	16
22	2.6 Multi-Messenger Dark Matter	18
23	CHAPTER 3 MULTIMESSENGER ASTROPHYSICS: DETECTING HIGH EN-	
24	ERGY NEUTRAL MESSENGERS	21
25	3.1 Introduction	21
26	3.2 Charged Particles in a Medium	21
27	3.3 Photons (γ)	22
28	3.4 Neutrinos (ν)	22
29	3.5 Opportunities to Combine for Dark Matter	22
30	CHAPTER 4 HIGH ALTITUDE WATER CHERENKOV (HAWC) OBSERVATORY .	24
31	4.1 The Detector	24
32	4.2 Events Reconstruction and Data Acquisition	24
33	4.3 Remote Monitoring	24
34	CHAPTER 5 ICECUBE NEUTRINO OBSERVATORY	25
35	5.1 The Detector	25
36	5.2 Events Reconstruction and Data Acquisition	25
37	5.3 Northern Test Site	25
38	CHAPTER 6 COMPUTATIONAL TECHNIQUES IN PARTICLE ASTROPHYSICS .	26
39	6.1 Neural Networks for Gamma/Hadron Separation	26
40	6.2 Parallel Computing for Dark Matter Analyses	26
41	CHAPTER 7 GLORY DUCK	27
42	7.1 Dataset and Background	27
43	7.2 Analysis	29
44	7.3 HAWC Results	34
45	7.4 Glory Duck Combined Results	35
46	7.5 Appendix: HAWC Systematics	38

47	7.6 <i>J</i> -factor distributions	43
48	7.7 Discussion and Conclusions	47
49	CHAPTER 8 NU DUCK	50
50	BIBLIOGRAPHY	51

LIST OF TABLES

<p>52 Table 7.1 Summary of the relevant properties of the dSphs used in the present work. 53 Column 1 lists the dSphs. Columns 2 and 3 present their heliocentric distance 54 and galactic coordinates, respectively. Columns 4 and 5 report the J-factors of 55 each source given from the \mathcal{GS} and \mathcal{B} independent studies and their estimated 56 $\pm 1\sigma$ uncertainties. The values $\log_{10} J$ (\mathcal{GS} set) [30] correspond to the mean 57 J-factor values for a source extension truncated at the outermost observed star. 58 The values $\log_{10} J$ (\mathcal{B} set) [31] are provided for a source extension at the tidal 59 radius of each dSph. Bolded sources are within HAWC's field of view and 60 provided to the Glory Duck analysis.</p>	31
<p>61 Table 7.2 Summary of dSph observations by each experiment used in this work. A 62 ‘-’ indicates the experiment did not observe the dSph for this study. For 63 Fermi-LAT, the exposure at 1 GeV is given. For HAWC, $\Delta\theta$ is the absolute 64 difference between the source declination and HAWC latitude. HAWC is more 65 sensitive to sources with smaller $\Delta\theta$. For IACTs, we show the zenith angle 66 range, the total exposure, the energy range, the angular radius θ of the signal or 67 ON region, the ratio of exposures between the background-control (OFF) and 68 signal (ON) regions (τ), and the significance of gamma-ray excess in standard 69 deviations, σ.</p>	32
<p>70 Proof I know how to include</p>	

LIST OF FIGURES

<p>72 Figure 2.1 Rotation curve fit to NGC 6503 from [7]. Dashed line is the contribution 73 from visible matter. Dotted curves are from gas. Dash-dot curves are from 74 dark matter (DM). Solid line is the composite contribution from all matter 75 and DM sources. Data are indicated with bold dots with error bars. Data 76 agree strongly with a matter + DM composite prediction.</p> <p>77 Figure 2.2 Light from distant galaxy is bent in unique ways depending on the distribution 78 of mass between the galaxy and Earth. Yellow dashed lines indicate where 79 the light would have gone if the matter were not present [8].</p> <p>80 Figure 2.3 (left) Optical image of galactic cluster 1E0657-558. (right) X-ray image of the 81 cluster with redder meaning hotter and higher baryon density. (both) Green 82 contours are reconstruction of gravity contours from weak lensing. White 83 rings are the best fit mass maxima at 68.3%, 95.5%, and 99.7% confidence. 84 The matter maxima of the clusters are clearly separated from x-ray maxima. [9]</p> <p>85 Figure 2.4 Plank CMB sky. Sky map features small variations in temperature in primor- 86 dial light. These anisotropies are used to make inferences about the universe's 87 energy budget and developmental history. [10]</p> <p>88 Figure 2.5 Observed Cosmic Microwave Background power spectrum as a function of 89 multipole moment from Plank [10]. Blue line is best fit model from ΛCDM. 90 Red points and lines are data and error, respectively.</p> <p>91 Figure 2.6 Predicted power spectra of CMB for different $\Omega_m h^2$ values for fixed baryon 92 density from [11]. (left) Low $\Omega_m h^2$ increases the prominence of first and 93 second peaks. (middle) $\Omega_m h^2$ is most similar to the observed power spectrum. 94 The second and third peaks are similar in height. (right) $\Omega_m h^2$ is large which 95 suppresses the first peak and raises the prominence of the third peak.</p> <p>96 Figure 2.7 The Standard Model (SM) of particle physics. Figure taken from http://www.quantumdiaries.org/2014/03/14/the-standard-model-a-beautiful-but-flawed-theory/</p> <p>99 Figure 2.8 Simplified Feynman diagram demonstrating with different ways DM can 100 interact with SM particles. The 'X's refer to the DM particles whereas the 101 SM refer to fundamental particles in the SM. The large circle in the center 102 indicates the vertex of interaction and is purposely left vague. The colored 103 arrows refer to different directions of time as well as their respective labels. 104 The arrows indicate the initial and final state of the DM -SM interaction in time.</p>	<p style="text-align: right;">5</p> <p style="text-align: right;">7</p> <p style="text-align: right;">8</p> <p style="text-align: right;">9</p> <p style="text-align: right;">10</p> <p style="text-align: right;">10</p> <p style="text-align: right;">12</p> <p style="text-align: right;">13</p>
---	---

105	Figure 2.9 A single jet event in ATLAS detector from 2017 [16]. Jet momentum was 106 observed to be 1.9 TeV. Missing transverse momentum was observed to be 107 1.9 TeV compared to the initial transverse momentum of the event was 0. 108 Implied MET is traced by a red dashed line in event display.	14
109	Figure 2.10 More detailed pseudo-Feynman diagram of particle cascade from dark matter 110 annihilation into 2 quarks. The quarks hadronize and down to stable particles 111 like γ or the anti-proton (p^-). Diagram pulled from ICRC 2021 presentation 112 on DM annihilation search [17].	15
113	Figure 2.11 Dark Matter (DM) decay spectrum for $b\bar{b}$ initial state and γ final state. Redder 114 spectra are for larger DM masses. Bluer spectra are light DM masses. x is a 115 unitless factor defined as the ratio of the mass of DM, m_χ , and the final state 116 particle energy E_γ . Figure from [19].	17
117	Figure 2.12 Different dark matter density profiles compared. Some models produce ex- 118 ceptionally large densities at small r [20].	18
119	Figure 2.13 The Milky Way Galaxy in photons (γ) and neutrinos (ν) [22]. The Galactic 120 center is at $l=0^\circ$ and is the brightest region in all panels. (top) An Optical 121 color image of the Milky Way galaxy seen from Earth. Clouds of gas and dust 122 obscure some light from stars. (2nd down) Integrated flux of γ -rays observed 123 by the Fermi-LAT telescope [23]. (middle) Expected neutrino emission 124 that corresponds with Fermi-LAT observations. (2nd up) Expected neutrino 125 emission profile after considering detector systematics of IceCube. (bottom) 126 Observed neutrino emission from region of the galactic plane. Substantial 127 neutrino emission was detected.	19
128	Figure 2.14 Dark Matter annihilation spectra for different final state particle and standard 129 model annihilation channels [24]. Photons (red), e^\pm (green), \bar{p} (blue), ν (black).	20
130	Figure 3.1 TODO: Show a nuclear reactor with cherenkov radiation[NEEDS A SOURCE][FACT 131 CHECK THIS]	22
132	Figure 3.2 TODO: absorption spectrum of liquid and solid water[NEEDS A SOURCE][FACT 133 CHECK THIS]	23

134	Figure 7.1 Illustration of the combination technique showing a comparison between 135 $-2 \ln \lambda$ provided by four instruments (colored lines) from the observation 136 of the same dSph without any J nuisance and their sum, <i>i.e.</i> the resulting 137 combined likelihood (thin black line). According to the test statistics of 138 Equation (7.6), the intersection of the likelihood profiles with the line $-2 \ln \lambda$ 139 = 2.71 indicates the 95% C.L. upper limit on $\langle \sigma v \rangle$. The combined likeli- 140 hood (thin black line) shows a smaller value of upper limit on $\langle \sigma v \rangle$ than 141 those derived by individual instruments. We also show the uncertainties on 142 the J -factor affects the combined likelihood and degrade the upper limit on 143 $\langle \sigma v \rangle$ (thick black line). All likelihood profiles are normalized so that the 144 global minimum $\langle \sigma v \rangle$ is 0. We note that each profile depends on the observa- 145 tional conditions in which a target object was observed. The sensitivity of a 146 given instrument can be degraded and the upper limits less constraining if the 147 observations are performed in non optimal conditions such as a high zenith 148 angle or a short exposure time.	34
149	Figure 7.2 HAWC upper limits at 95% confidence level on $\langle \sigma v \rangle$ versus DM mass for 150 seven annihilation channels, using the set of J -factors from Ref. [29] The 151 solid line represents the observed combined limit. Dashed lines represent 152 limits from individual dSphs.	36
153	Figure 7.3 HAWC Brazil bands at 95% confidence level on $\langle \sigma v \rangle$ versus DM mass for 154 seven annihilation channels with J -factors from \mathcal{GS} [29]. The solid line 155 represents the combined limit from 13 dSphs. The dashed line is the expected 156 limit. The green band is the 68% containment. The yellow band is the 95% 157 containment.	37
158	Figure 7.4 Upper limits at 95% confidence level on $\langle \sigma v \rangle$ in function of the DM mass for 159 eight annihilation channels, using the set of J factors from Ref. [29] (\mathcal{GS} set 160 in Table 7.1). The black solid line represents the observed combined limit, 161 the black dashed line is the median of the null hypothesis corresponding 162 to the expected limit, while the green and yellow bands show the 68% and 163 95% containment bands. Combined upper limits for each individual detector 164 are also indicated as solid, colored lines. The value of the thermal relic 165 cross-section in function of the DM mass is given as the red dotted-dashed 166 line [36].	39
167	Figure 7.5 Same as Fig. 7.4, using the set of J factors from Ref. [31, 35] (\mathcal{B} set in Table 7.1). 40	
168	Figure 7.6 Comparisons of the combined limits at 95% confidence level for each of the 169 eight annihilation channels when using the J factors from Ref. [29] (\mathcal{GS} set in 170 Table 7.1), plain lines, and the J factor from Ref. [31, 35] (\mathcal{B} set in Table 7.1), 171 dashed lines. The cross-section given by the thermal relic is also indicated [36]. 41	

172	Figure 7.7	Comparisons of the combined limits at 95% confidence level for a point source analysis and extended source using [29] \mathcal{GS} J-factor distributions and PPPC [28] annihilation spectra. Shown are the limits for Segue1 which will have the most significant impact on the combined limit. 6 of the 7 DM annihilation channels are shown. Solid lines are extended source studies. Dashed lines are point source studies. Overall, the extended source analysis improves the limit by a factor of 2.	42
179	Figure 7.8	Same as Fig. 7.7 on Coma Berenices. This dSph also contributes significantly to the limit. The limits are identical in this case.	43
181	Figure 7.9	Comparison of combined limits when correcting for HAWC's pointing systematic. All DM annihilation channels are shown. The solid black line is the ratio between published limit to the declination corrected limit. The blue solid line or "Combined_og" represented the limits computed for Glory Duck. The solid orange line or "Combined_ad" represented the limits computed after correcting for the pointing systematic.	44
187	Figure 7.10	Comparisons between the J -factors versus the angular radius for the computation of J factors from Ref. [29] (\mathcal{GS} set in Table 7.1) in blue and for the computation from Ref. [31, 35] (\mathcal{B} set in Tab. 7.1) in orange. The solid lines represent the central value of the J -factors while the shaded regions correspond to the 1σ standard deviation.	46
192	Figure 7.11	Comparisons between the J -factors versus the angular radius for the computation of J factors from Ref. [29] (\mathcal{GS} set in Tab. 7.1) in blue and for the computation from Ref. [31, 35] (\mathcal{B} set in Tab. 7.1) in orange. The solid lines represent the central value of the J -factors while the shaded regions correspond to the 1σ standard deviation.	47

LIST OF ABBREVIATIONS

- 198 **MSU** Michigan State University
199 **LANL** Los Alamos National Laboratory
200 **DM** Dark Matter
201 **SM** Standard Model
202 **HAWC** High Altitude Water Cherenkov Observatory

203

CHAPTER 1

INTRODUCTION

204 Is the text not rendering right? Ah ok it knows im basically drafting the doc still

CHAPTER 2

205

DARK MATTER IN THE COSMOS

206 **2.1 Introduction**

207 The dark matter problem can be summarized in part by the following thought experiment.

208 Let us say you are the teacher for an elementary school classroom. You take them on a field
209 trip to your local science museum and among the exhibits is one for mass and weight. The exhibit
210 has a gigantic scale, and you come up with a fun problem for your class.

211 You ask your class, "What is the total weight of the classroom? Give your best estimation to
212 me in 30 minutes, and then we'll check your guess on the scale. If your guess is within 10% of the
213 right answer, we will stop for ice cream on the way back."

214 The students are ecstatic to hear this, and they get to work. The solution is some variation of
215 the following strategy. The students should give each other their weight or best guess if they do
216 not know. Then, all they must do is add each student's weight and get a grand total for the class.
217 The measurement on the giant scale should show the true weight of the class. When comparing
218 the measured weight to your estimation, multiply the measurement by 1.0 ± 0.1 to get the $\pm 10\%$
219 tolerances for your estimation.

220 Two of your students, Sandra and Mario, return to you with a solution.

221 They say, "We weren't sure of everyone's weight. We used 65 lbs. for the people we didn't
222 know and added everyone who does know. There are 30 of us, and we got 2,000 lbs.! That's a ton!"

223 You estimated 1,900 lbs. assuming the average weight of a student in your class was 60 lbs.
224 So, you are pleased with Sandra's and Mario's answer. You instruct your students to all gather on
225 the giant scale and read off the weight together. To all your surprise, the scale reads *10,000 lbs.*!
226 10,000 is significantly more than a 10% error from 2,000. In fact, it is approximately 5 times more
227 massive than either your or your students' estimates. You think to yourself and conclude there
228 must be something wrong with the scale. You ask an employee to check the scale and verify it is
229 well calibrated. They confirm that the scale is in working order. You weigh a couple of students
230 individually to assess that the scale is well calibrated. Sandra weighs 59 lbs., and Mario weighs

231 62 lbs., typical weights for their age. You then weigh each student individually and see that their
232 weights individually do not deviate greatly from 60 lbs. So, where does all the extra weight come
233 from?

234 This thought experiment serves as an analogy to the Dark Matter problem. The important
235 substitution to make however is to replace the students with stars and the classroom with a galaxy,
236 say the Milky Way. Individually the mass of stars is well measured and defined with the Sun as our
237 nearest test case. However, when we set out to measure the mass of a collection of stars as large as
238 galaxies, our well-motivated estimation is wildly incorrect. There simply is no way to account for
239 this discrepancy except without some unseen, or dark, contribution to mass and matter in galaxies.
240 I set out in my thesis to narrow the possibilities of what this Dark Matter could be.

241 This chapter is organized like the following... **TODO: Text should look like ... Chapter x has**
242 **blah blah blah.**

243 2.2 Dark Matter Basics

244 Presently, a more compelling theory of cosmology that includes Dark Matter (DM) in order
245 to explain a variety of observations is Λ Cold Dark Matter, or Λ CDM. I present the evidence
246 supporting Λ CDM in Section 2.3 yet discuss the conclusions of the Λ CDM model here. According
247 to Λ CDM fit to observations on the Cosmic Microwave Background (CMB), DM is 26.8% of the
248 universe's current energy budget. Baryonic matter, stuff like atoms, gas, and stars, contributes to
249 4.9% of the universe's current energy budget [1, 2, 3].

250 DM is dark; it does not interact readily with light at any wavelength. DM also does not interact
251 noticeably with the other standard model forces (Strong and Weak) at a rate that is readily observed
252 [3]. DM is cold, which is to say that the average velocity of DM is below relativistic speeds [1].
253 'Hot' DM would not likely manifest the dense structures we observe like galaxies, and instead
254 would produce much more diffuse galaxies than what is observed [3, 1]. DM is old; it played a
255 critical role in the formation of the universe and the structures within it [1, 2].

256 Observations of DM have so far been only gravitational. The parameter space available to what
257 DM could be therefore is extremely broad. The broad DM parameter space is iteratively tested in

258 DM searches by supposing a hypothesis that has not yet been ruled out and performing observations
259 to test them. When the observations yield a null result, the parameter space is constrained further.
260 I present some approaches for DM searches in Section 2.4.

261 **2.3 Evidence for Dark Matter**

262 Dark Matter (DM) has been a looming problem in physics for almost 100 years. Anomalies
263 have been observed by astrophysicists in galactic dynamics as early as 1933 when Fritz Zwicky
264 noticed unusually large velocity dispersion in the Coma cluster. Zwicky's measurement was the
265 first recorded to use the Virial theorem to measure the mass fraction of visible and invisible matter
266 in celestial bodies [4]. From Zwicky in [5], "*If this would be confirmed, we would get the surprising*
267 *result that dark matter is present in much greater amount than luminous matter.*" Zwicky's and
268 others' observation did not instigate a crisis in astrophysics because the measurements did not
269 entirely conflict with their understanding of galaxies [4]. In 1978, Rubin, Ford, and Norbert
270 measured rotation curves for ten spiral galaxies [6]. Rubin et al.'s 1978 publication presented a
271 major challenge to the conventional understanding of galaxies that could no longer be dismissed by
272 measurement uncertainties. Evidence has been mounting ever since for this exotic form of matter.
273 The following subsections provide three compelling pieces of evidence in support of the existence
274 of DM.

275 **2.3.1 First Clues: Stellar Velocities**

276 Zwicky, and later Rubin, measured the stellar velocities of various galaxies to estimate their
277 virial mass. The Virial Theorem upon which these observations are interpreted is written as

$$2T + V = 0. \quad (2.1)$$

278 Where T is the kinetic energy and V is the potential energy in a self-gravitating system. The
279 classical Newton's law of gravity from stars and gas was used for gravitational potential modeled in
280 the observed galaxies:

$$V = -\frac{1}{2} \sum_i \sum_{j \neq i} \frac{m_i m_j}{r_{ij}}. \quad (2.2)$$

281 Zwicky et al. measured just the velocities of stars apparent in optical wavelengths [5]. Rubin et al.
 282 added by measuring the velocity of the hydrogen gas via the 21 cm emission line of Hydrogen [6].
 283 The velocities of the stars and gas are used to infer the total mass of galaxies and galaxy clusters
 284 via Equation (2.1). An inferred mass is obtained from the luminosity of the selected sources. The
 285 two inferences are compared to each other as a luminosity to mass ratio which typically yielded [1]

$$\frac{M}{L} \sim 400 \frac{M_{\odot}}{L_{\odot}} \quad (2.3)$$

286 M_{\odot} and L_{\odot} referring to stellar mass and stellar luminosity, respectively. These ratios clearly indicate
 287 a discrepancy in apparent light and mass from stars and gas and their velocities.

288 Rubin et al. [6] demonstrated that the discrepancy was unlikely to be an underestimation of
 289 the mass of the stars and gas. The inferred "dark" mass was up to 5 times more than the luminous
 290 mass. This dark mass also needed to extend well beyond the extent of the luminous matter.

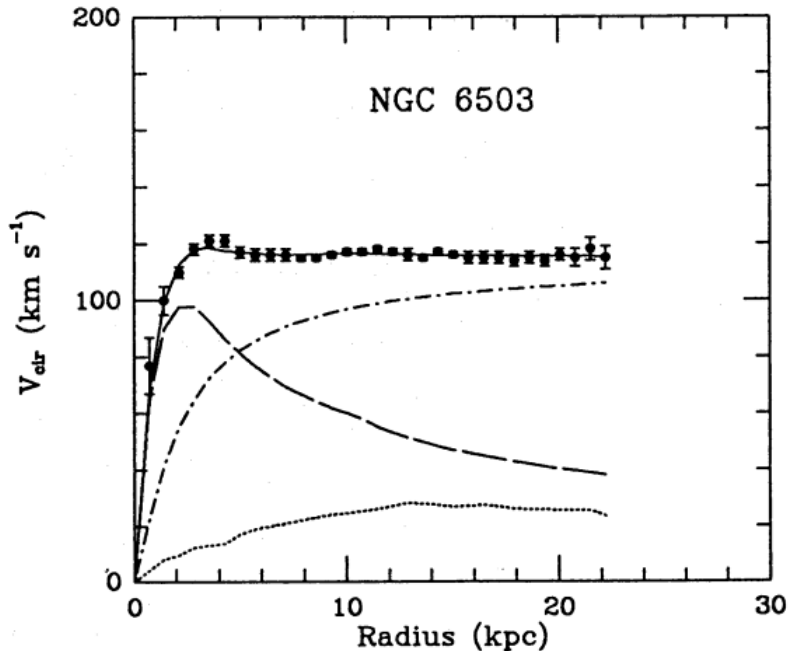


Figure 2.1 Rotation curve fit to NGC 6503 from [7]. Dashed line is the contribution from visible matter. Dotted curves are from gas. Dash-dot curves are from dark matter (DM). Solid line is the composite contribution from all matter and DM sources. Data are indicated with bold dots with error bars. Data agree strongly with a matter + DM composite prediction.

291 Figure 2.1 features one of many rotation curves plotted from the stellar velocities within galaxies.

292 The measured rotation curves mostly feature a flattening of velocities at higher radius which is not
293 expected if the gravity was only coming from gas and luminous matter. The extension of the
294 flat velocity region also indicates that the DM is distributed far from the center of the galaxy.
295 Modern velocity measurements include significantly larger objects, galactic clusters, and smaller
296 objects, dwarf galaxies. Yet, measurements along this regime are leveraging the Virial theorem
297 with Newtonian potential energies. We know Newtonian gravity is not a comprehensive description
298 of gravity. New observational techniques have been developed since 1978, and those are discussed
299 in the following sections.

300 **2.3.2 Evidence for Dark Matter: Gravitational Lensing**

301 Modern evidence for dark matter comes from new avenues beyond stellar velocities. Grav-
302 itational lensing from DM is a new channel from general relativity. General relativity predicts
303 aberrations in light caused by massive objects. In recent decades we have been able to measure the
304 lensing effects from compact objects and DM halos. Figure 2.2 shows how different massive ob-
305 jects change the final image of a faraway galaxy resulting from gravitational lensing. Gravitational
306 lensing developed our understanding of dark matter in two important ways.

307 Gravitational lensing provides additional compelling evidence for DM. The observation of two
308 merging galactic clusters in 2006, shown in Figure 2.3, provided a compelling argument for DM
309 outside the Standard Model. These clusters merged recently in astrophysical time scales. Galaxies
310 and star cluster have mostly passed by each other as the likelihood of their collision is low. Therefore,
311 these massive objects will mostly track the highest mass, dark and/or baryonic, density. Yet, the
312 intergalactic gas is responsible for the majority of the baryonic mass in the systems [4]. These gas
313 bodies will not phase through and will heat up as they collide together. The hot gas is located via
314 x-ray emission from the cluster. Two observations of the clusters were performed independently of
315 each other.

316 The first was the lensing of light around the galaxies due to their gravitational influences.
317 When celestial bodies are large enough, the gravity they exert bends space and time itself. The
318 warped space-time lenses light and will deflect in an analogous way to how glass lenses will bend

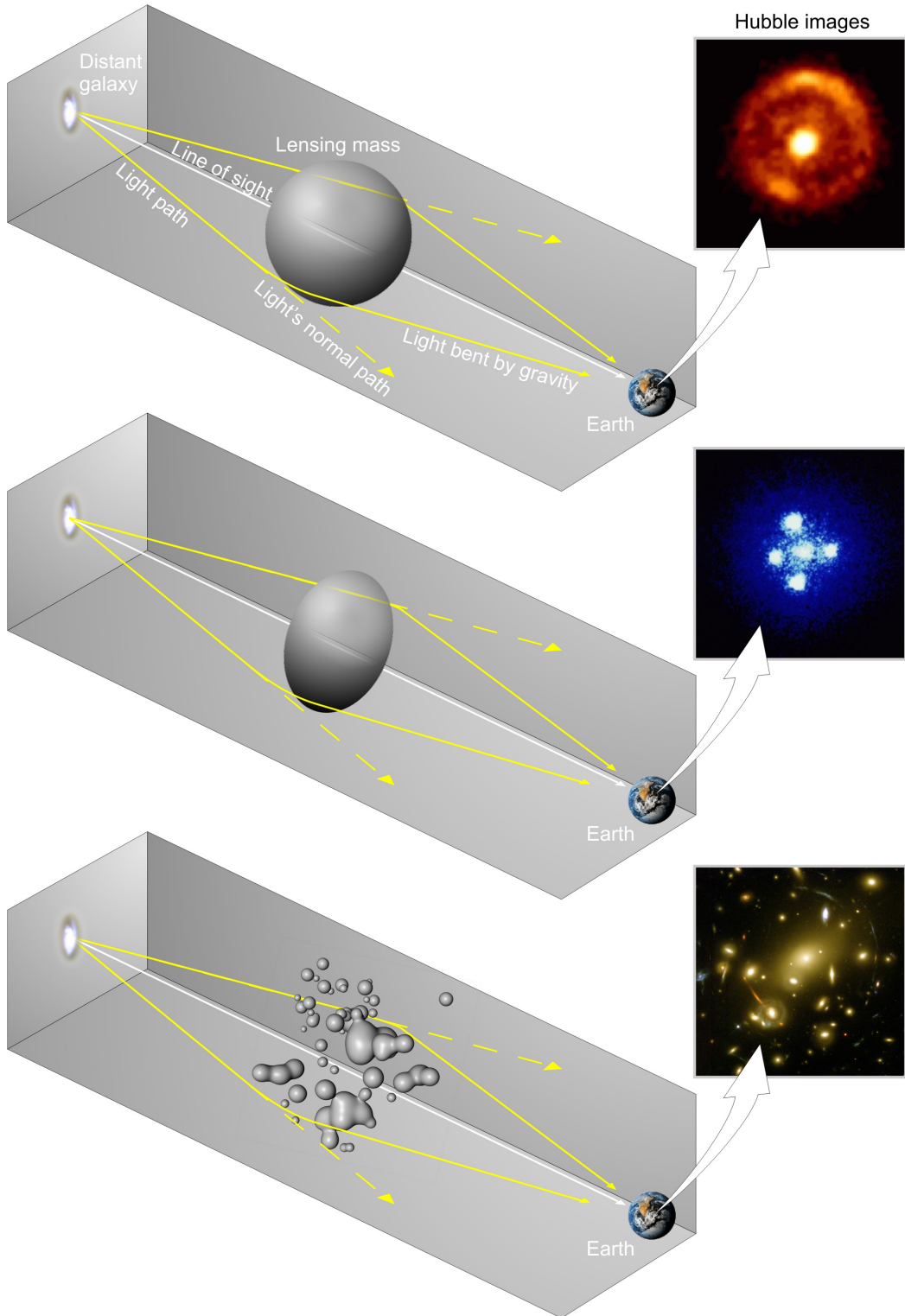


Figure 2.2 Light from distant galaxy is bent in unique ways depending on the distribution of mass between the galaxy and Earth. Yellow dashed lines indicate where the light would have gone if the matter were not present [8].

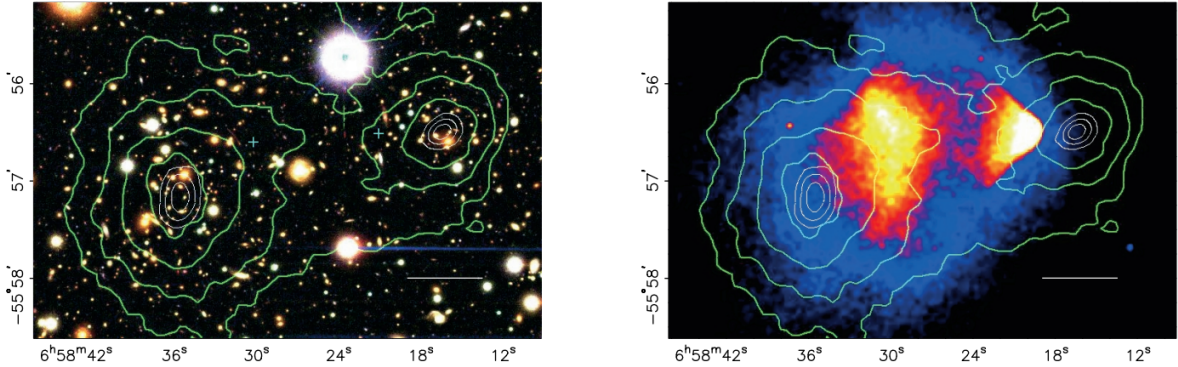


Figure 2.3 (left) Optical image of galactic cluster 1E0657-558. (right) X-ray image of the cluster with redder meaning hotter and higher baryon density. (both) Green contours are reconstruction of gravity contours from weak lensing. White rings are the best fit mass maxima at 68.3%, 95.5%, and 99.7% confidence. The matter maxima of the clusters are clearly separated from x-ray maxima. [9]

319 light, see Figure 2.2. With a sufficient understanding of light sources behind a massive object, we
 320 can reconstruct the contours of the gravitational lenses. The gradient of the contours shown in
 321 Figure 2.3 then indicates how dense the matter is and where it is.

322 The x-ray emission can then be observed from the clusters. Since these galaxies are mostly gas
 323 and are merging, then the gas should be getting hotter. If they are merging, the x-ray emissions
 324 should be the strongest where the gas is mostly moving through each other. Hence, X-ray emission
 325 maps out where the gas is in the merging galaxy cluster.

326 The lensing and x-ray observations were done on the Bullet cluster featured on Figure 2.3.
 327 The x-ray emissions do not align with the gravitational contours from lensing. The incongruence
 328 in mass density and baryon density suggests that there is a lot of matter somewhere that does
 329 not interact with light. Moreover, this dark matter cannot be baryonic [9]. The Bullet Cluster
 330 measurement did not really tell us what DM is exactly, but it did give the clue that DM also does
 331 not interact with itself very strongly. If DM did interact strongly with itself, then it would have been
 332 more aligned with the x-ray emission [9]. There have been follow-up studies of galaxy clusters with
 333 similar results. The Bullet Cluster and others like it provide a persuasive case against something
 334 possibly amiss in our gravitational theories.

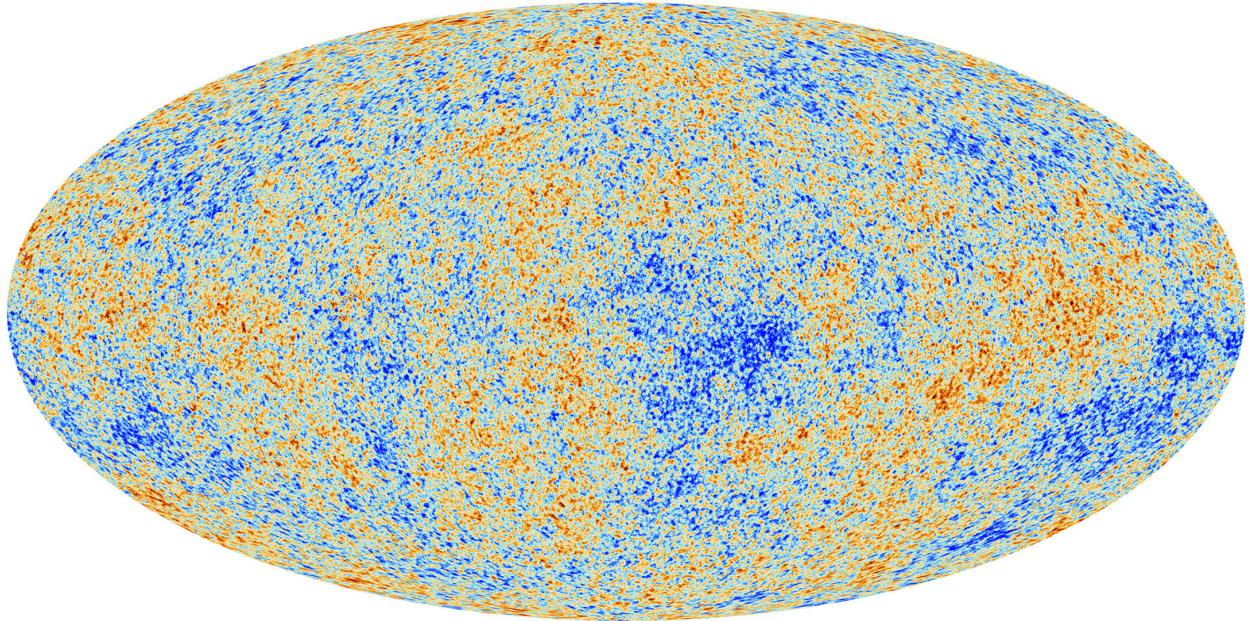


Figure 2.4 Plank CMB sky. Sky map features small variations in temperature in primordial light. These anisotropies are used to make inferences about the universe’s energy budget and developmental history. [10]

335 **2.3.3 Evidence for Dark Matter: Cosmic Microwave Background**

336 The Cosmic Microwave Background (CMB) is the primordial light from the early universe
337 when Hydrogen atoms formed from the free electron and proton soup in the early universe. The
338 CMB is the earliest light we can observe; released when the universe was about 380,000 years old.
339 Then we look at how the simulated universes look like compared to what we see. Figure 2.4 is the
340 most recent CMB image from the Plank satellite after subtracting the average value and masking the
341 galactic plane [10]. Redder regions indicate a slightly hotter region in the CMB, and blue indicates
342 colder. The intensity variations are on the order of 1 in 1000 with respect to the average value.

343 The Cosmic Microwave Background shows that the universe had DM in it from an incredibly
344 early stage. To measure the DM, Dark Energy, and matter fractions of the universe from the CMB,
345 the image is analyzed into a power spectrum, which shows the amplitude of the fluctuations as
346 a function of spherical multipole moments. Λ CDM provides the best fit to the power spectra of
347 the CMB as shown in Figure 2.5. The CMB power spectrum is quite sensitive to the fraction
348 of each energy contribution in the early universe. Low l modes are dominated by variations
349 in gravitational potential. Intermediate l emerge from oscillations in photon-baryon fluid from

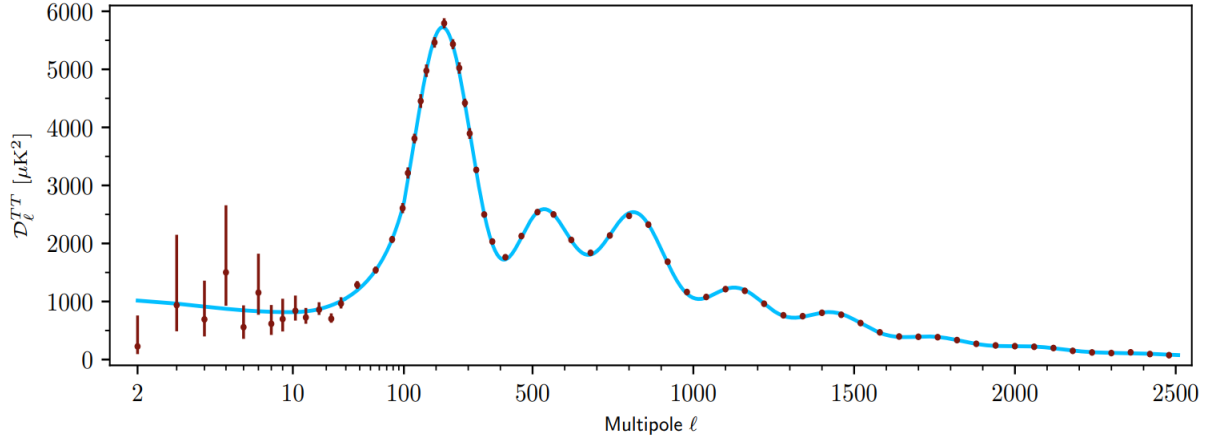


Figure 2.5 Observed Cosmic Microwave Background power spectrum as a function of multipole moment from Plank [10]. Blue line is best fit model from Λ CDM. Red points and lines are data and error, respectively.

350 competing baryon pressures and gravity. High l is a damped region from the diffusion of photons
 351 during electron-proton recombination. [1]

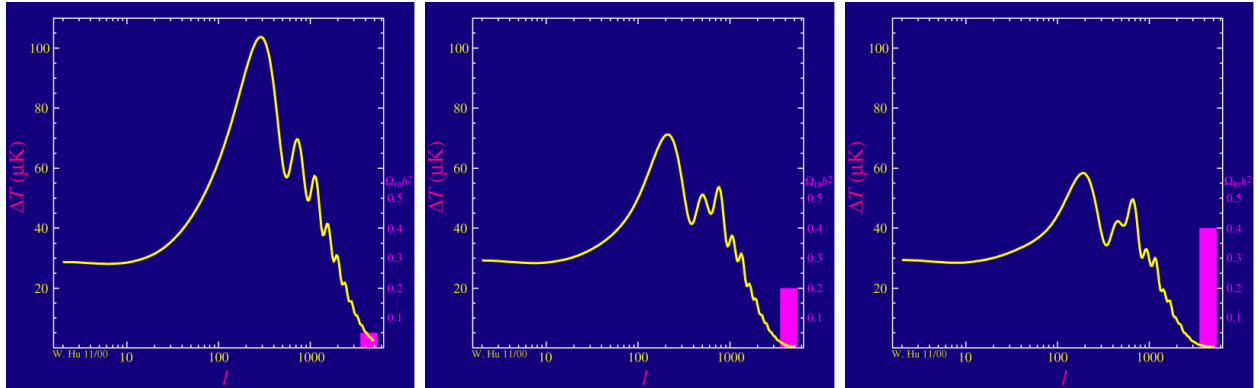


Figure 2.6 Predicted power spectra of CMB for different $\Omega_m h^2$ values for fixed baryon density from [11]. (left) Low $\Omega_m h^2$ increases the prominence of first and second peaks. (middle) $\Omega_m h^2$ is most similar to the observed power spectrum. The second and third peaks are similar in height. (right) $\Omega_m h^2$ is large which suppresses the first peak and raises the prominence of the third peak.

352 The harmonics would look quite different for a universe with less DM. Figure 2.6 demonstrates
 353 the effect $\Omega_m h^2$ has on the expected power spectrum for fixed baryon matter density. [11] Sweeping
 354 $\Omega_m h^2$ in this way clearly shows the effect dark matter has on the CMB power spectrum. The
 355 observations fit well with the Λ CDM model, and the derived fractions are as follows. The matter
 356 fraction: $\Omega_m = 0.3153$; and the baryon fraction: $\Omega_b = 0.04936$ [10]. Plank's observations also
 357 provide a measure of the Hubble constant, H_0 . H_0 especially has seen a growing tension in the

358 past decade that continues to deepened with observations from instruments like the James Webb
359 Telescope [12, 13]. As Hubble tensions deepen, we may find that perhaps Λ **CDM**, despite its
360 successes, is missing some critical physics.

361 Overall, the Newtonian motion of stars in galaxies, weak lensing from galactic clusters, and
362 power spectra from primordial light form a compelling body of research in favor of dark matter.
363 It takes another leap of theory and experimentation to make observations of DM that are non-
364 gravitational in nature. In Section 2.3, the evidence for DM implies strongly that the DM is matter
365 and not a lost parameter in the gravitational fields between massive objects. Finally, if we take one
366 axiom: that this matter has quantum behavior, such as being described by some Bohr wavelength
367 and abiding by some fermion or boson statistics; then we arrive at particle dark matter. One particle
368 DM hypothesis is the Weakly Interacting Massive Particle (WIMP). This DM candidate theory is
369 discussed further in the next section and is the focus of this thesis.

370 **2.4 Searching for Dark Matter: Particle DM**

371 Section 2.4 shows the Standard Model of particle physics and is currently the most accurate
372 model for the dynamics of fundamental particles like electrons and photons. The current status
373 of the SM does not have a viable DM candidate. When looking at the standard model, we can
374 immediately exclude any charged particle because charged particles interact strongly with light.
375 Specifically, this will rule out the following charged, fundamental particles: $e, \mu, \tau, W, u, d, s, c, t, b$
376 and their corresponding antiparticles. Recalling from Section 2.2 that DM must be long-lived and
377 stable over the age of the universe which excludes all SM particles with decay half-lives at or shorter
378 than the age of the universe. The lifetime constraint additionally eliminates the Z and H bosons.
379 Finally, the candidate DM needs to be somewhat massive. Recall from Section 2.2 that DM is cold
380 or not relativistic through the universe. This eliminates the remaining SM particles: $\nu_{e,\mu,\tau}, g, \gamma$ as
381 DM candidates. Because there are no DM candidates within the SM, the DM problem strongly
382 hints to physics beyond the SM (BSM).

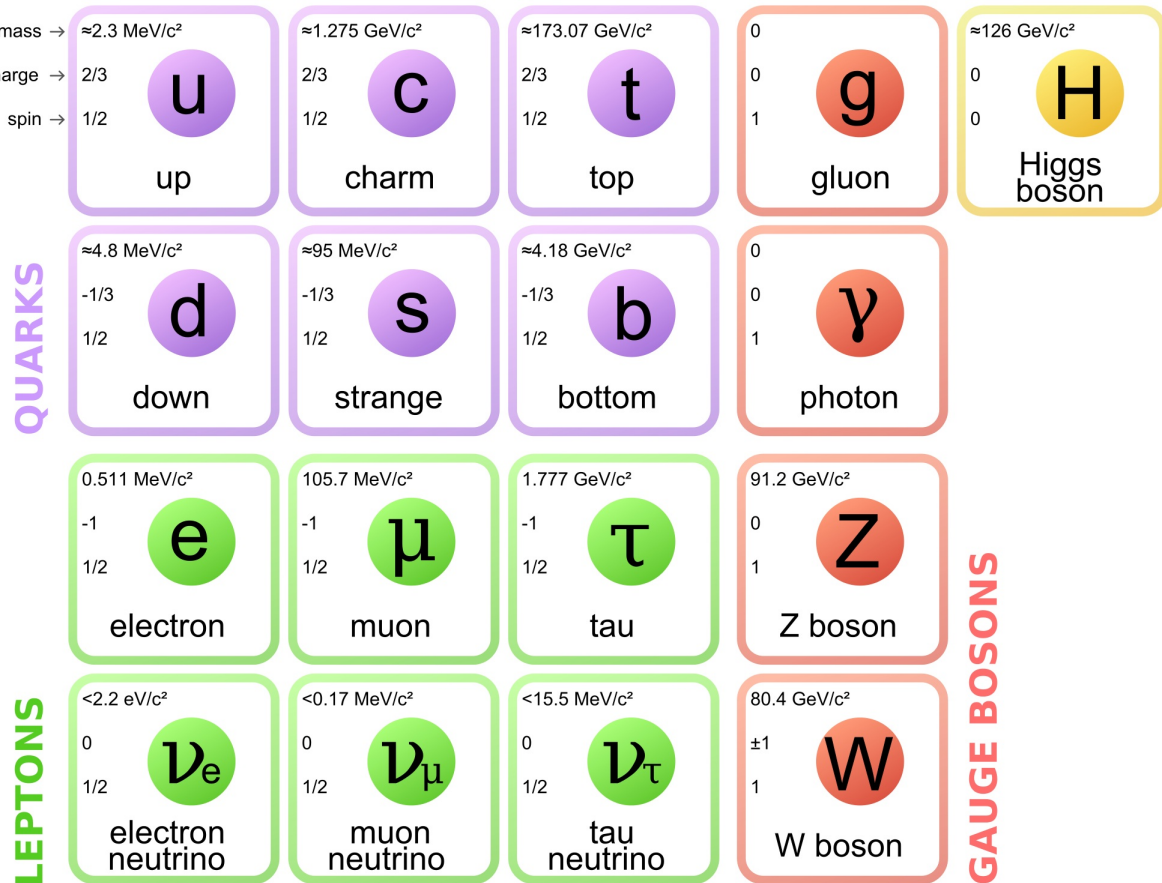


Figure 2.7 The Standard Model (SM) of particle physics. Figure taken from <http://www.quantumdiaries.org/2014/03/14/the-standard-model-a-beautiful-but-flawed-theory/>

383 2.4.1 Shake it, Break it, Make it

384 When considering DM that couples in some way with the SM, the interactions are roughly
 385 demonstrated by interaction demonstrated in Figure 2.8. The figure is a simplified Feynman
 386 diagram where the arrow of time represents the interaction modes of: **Shake it, Break it, Make it**.

387 **Shake it** refers to the direct detection of dark matter. Direct detection interactions start with
 388 a free DM particle and an SM particle. The DM and SM interact via elastic or inelastic collision
 389 and recoil away from each other. The DM remains in the dark sector and imparts some momentum
 390 onto the SM particle. The hope is that the momentum imparted onto the SM particle is sufficiently
 391 high enough to pick up with extremely sensitive instruments. Because we cannot create the DM in
 392 the lab, a direct detection experiment must wait until DM is incident on the detector. Most direct
 393 detection experiments are therefore placed in low-background environments with inert detection

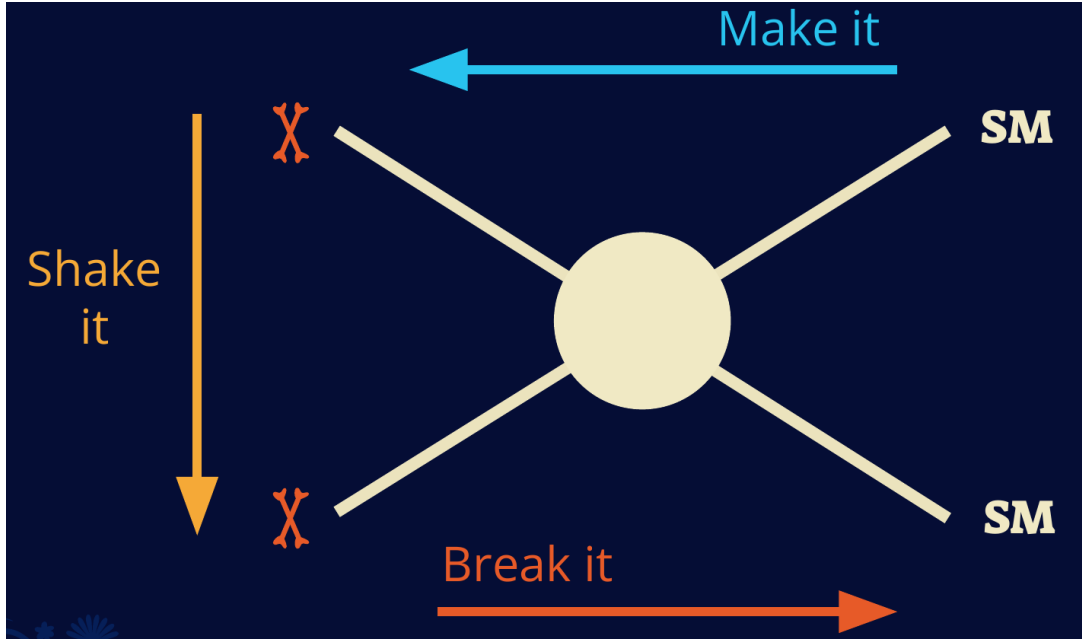


Figure 2.8 Simplified Feynman diagram demonstrating different ways DM can interact with SM particles. The 'X's refer to the DM particles whereas the SM refer to fundamental particles in the SM. The large circle in the center indicates the vertex of interaction and is purposely left vague. The colored arrows refer to different directions of time as well as their respective labels. The arrows indicate the initial and final state of the DM -SM interaction in time.

394 media like the noble gas Xenon. [14]

395 **Make it** refers to the production of DM from SM initial states. The experiment starts with
 396 particles in the SM. These SM particles are accelerated to incredibly high energies and then collide
 397 with each other. In the confluence of energy, DM hopefully emerges as a byproduct of the SM
 398 annihilation. Often it is the collider experiments that are energetic enough to hypothetically produce
 399 DM. These experiments include the world-wide collaborations ATLAS and CMS at CERN where
 400 proton collide together at extreme energies. The DM searches, however, are complex. DM likely
 401 does not interact with the detectors and lives long enough to escape the detection apparatus of
 402 CERN's colliders. This means any DM production experiment searches for an excess of events
 403 with missing momentum or energy in the events. An example event with missing transverse
 404 momentum is shown in Figure 2.9. The missing momentum with no particle tracks implies a
 405 neutral particle carried the energy out of the detector. However, there are other neutral particles
 406 in the SM, like neutrons or neutrinos, so any analysis has to account for SM signatures of missing

407 momentum. [15]

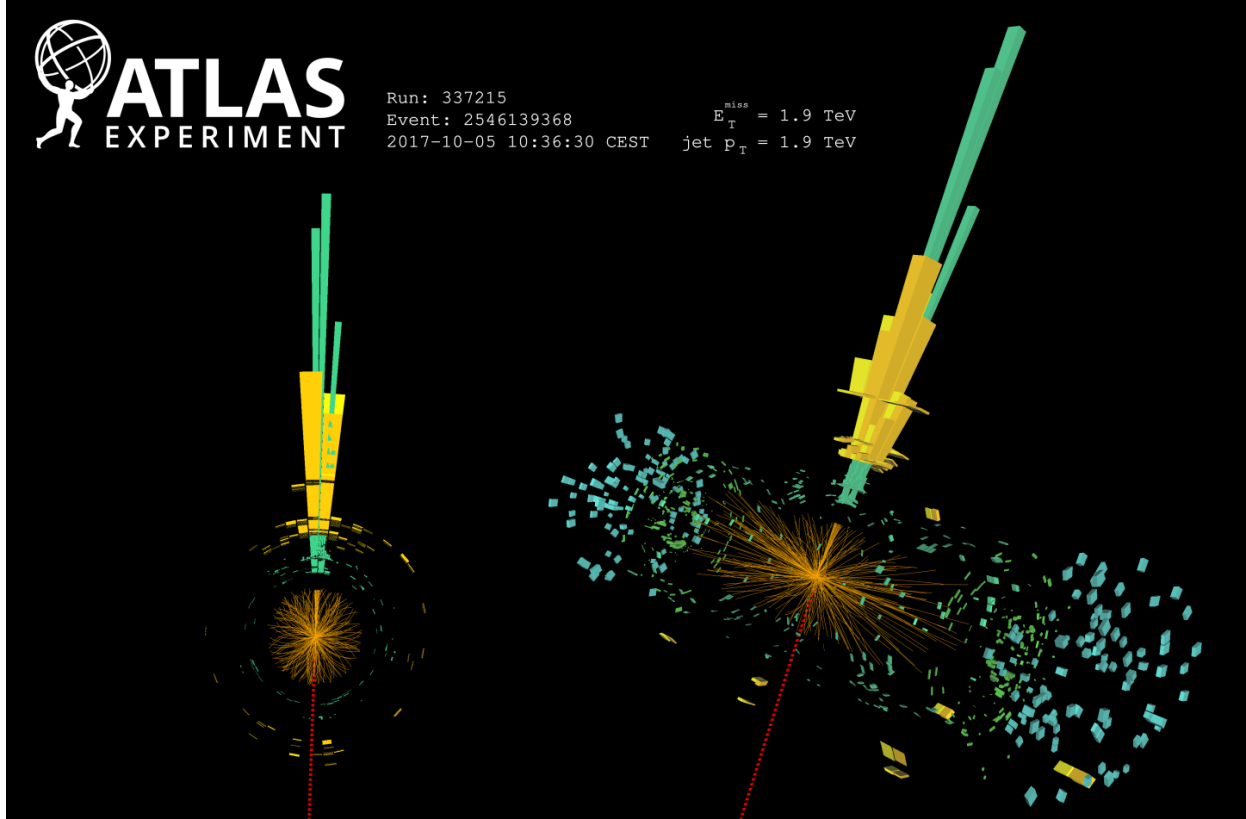


Figure 2.9 A single jet event in ATLAS detector from 2017 [16]. Jet momentum was observed to be 1.9 TeV. Missing transverse momentum was observed to be 1.9 TeV compared to the initial transverse momentum of the event was 0. Implied MET is traced by a red dashed line in event display.

408 2.4.2 Break it: Standard Model Signatures of Dark Matter through Indirect Searches

409 **Break it** refers to the creation of SM particles from the dark sector, and it is the primary focus
410 of this thesis. The interaction begins with DM or in the dark sector. The hypothesis is that this
411 DM will either annihilate with itself or decay and produce an SM byproduct. This method is
412 often referred to as the Indirect Detection of DM because we have no lab to directly control or
413 manipulate the DM. Therefore, most indirect DM searches are performed using observations of
414 known DM densities among the astrophysical sources. The strength is that we have the whole of the
415 universe and its 13.6-billion-year lifespan to use as a detector and particle accelerator. Additionally,
416 locations of dark matter are well cataloged since it was astrophysical observations that presented

417 the problem of DM in the first place.

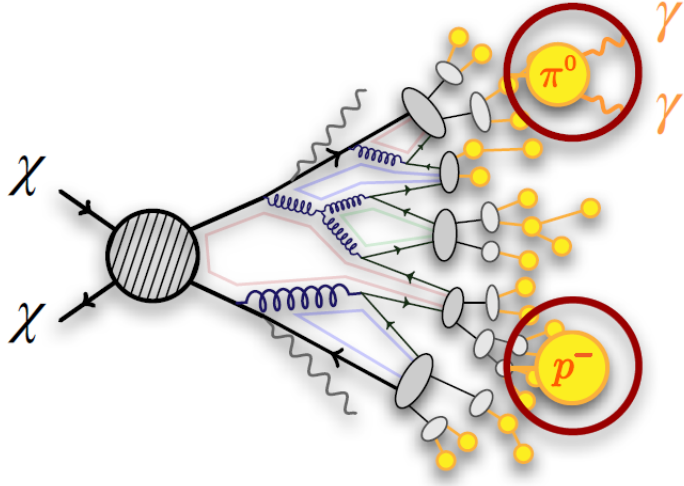


Figure 2.10 More detailed pseudo-Feynman diagram of particle cascade from dark matter annihilation into 2 quarks. The quarks hadronize and down to stable particles like γ or the anti-proton (p^-). Diagram pulled from ICRC 2021 presentation on DM annihilation search [17].

418 However, anything can happen in the universe. There are many difficult to deconvolve back-
419 grounds when searching for DM. One prominent example is the galactic center. We know the
420 galactic center has a large DM content because of stellar kinematics in our Milky Way and DM halo
421 simulations. Yet, any signal from the galactic center is challenging to parse apart from the extreme
422 environment of our supermassive black hole, unresolved sources, and diffuse emission from the
423 interstellar medium [18]. Despite the challenges, any DM model that yields evidence in the other
424 two observation methods, **Shake it or Make it** must be corroborated with indirect observations of
425 the known DM sources. Without corroborating evidence, DM observation in the lab is hard-pressed
426 to demonstrate that it is the model contributing to the DM seen at the universal scale.

427 In the case of WIMP DM, signals are described in terms of primary SM particles produced
428 from DM decay or annihilation. The SM initial state particles are then simulated down to stable
429 final states such as the γ , ν , p , or e which can traverse galactic lengths to reach Earth.

430 Figure 2.10 shows the quagmire of SM particles that emerges from SM initial states that are not
431 stable [17]. There are many SM particles with varying energies that can be produced in such an

432 interaction. For any arbitrary DM source and stable SM particle, the SM flux from DM annihilating
 433 to a neutral particle in the SM, ϕ , from a region in the sky is described by the following.

$$\frac{d\Phi_\phi}{dE_\phi} = \frac{\langle\sigma v\rangle}{8\pi m_\chi^2} \frac{dN_\phi}{dE_\phi} \times \int_{\text{source}} d\Omega \int_{l.o.s} \rho_\chi^2 dl(r, \theta') \quad (2.4)$$

434 In Equation (7.1), $\langle\sigma v\rangle$ is the velocity-weighted annihilation cross-section of DM to the SM. m_χ
 435 refers to the mass of DM, noted with Greek letter χ . $\frac{dN_\phi}{dE_\phi}$ is the N particle flux weighted by the
 436 particle energy. An example is provided in Figure 2.11 for the γ final state. The integrated terms
 437 are performed over the solid angle, $d\Omega$, and line of sight, l.o.s. ρ is the density of DM for a
 438 location (r, θ') in the sky. The terms left of the ' \times ' are often referred to as the particle physics
 439 component. The terms on the right are referred to as the astrophysical component. For decaying
 440 DM, the equation changes to...

$$\frac{d\Phi_\phi}{dE_\phi} = \frac{1}{4\pi\tau m_\chi} \frac{dN_\phi}{dE_\phi} \times \int_{\text{source}} d\Omega \int_{l.o.s} \rho_\chi dl(r, \theta') \quad (2.5)$$

441 In Equation (2.5), τ is the decay lifetime of the DM. Just as in Equation (7.1), the left and
 442 right terms are the particle physics and the astrophysical components respectively. The integrated
 443 astrophysical component of Equation (7.1) is often called the J-Factor. Whereas the integrated
 444 astrophysical component of Equation (2.5) is often called the D-Factor.

445 Exact DM $\text{DM} \rightarrow \text{SM SM}$ branching ratios are not known, so it is usually assumed to go 100%
 446 into an SM particle/anti-particle. Additionally, when a DM annihilation or decay produces one of
 447 the neutral, long-lived SM particles (ν or γ), the particle is traced back to a DM source. For DM
 448 above GeV energies, there are very few SM processes that can produce particles with such a high
 449 energy. Seeing such a signal would almost certainly be an indication of the presence of dark matter.
 450 Fortunately, the universe provides us with the largest volume and lifetime ever for a particle physics
 451 experiment.

452 2.5 Sources for Indirect Dark Matter Searches

453 The first detection of DM relied on optical observations. Since then, we have developed new
 454 techniques to find DM dense regions. As described in Section 2.3.1, many DM dense regions were
 455 through observing galactic rotation curves. Our Milky Way galaxy is among DM dense regions

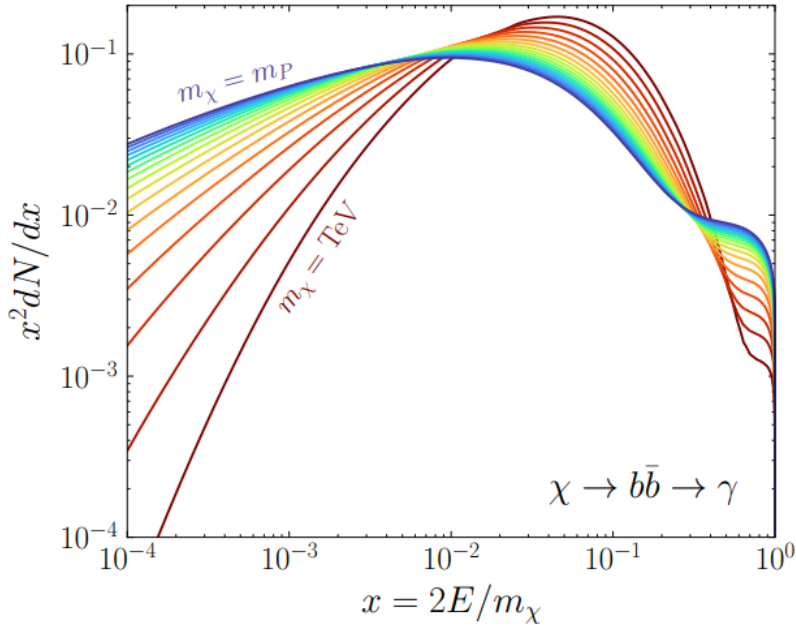


Figure 2.11 Dark Matter (DM) decay spectrum for $b\bar{b}$ initial state and γ final state. Redder spectra are for larger DM masses. Bluer spectra are light DM masses. x is a unitless factor defined as the ratio of the mass of DM, m_χ , and the final state particle energy E_γ . Figure from [19].

discovered, and it is the largest nearby DM dense region to look at. Additionally, the DM halo surrounding the Milky Way is clumpy [18]. There are regions in the DM halo of the Milky Way that have more DM than others that have captured gas over time. These sub-halos were dense enough to collapse gas and form stars. These apparent sub galaxies are known as dwarf spheroidal galaxies and are the main sources studied in this thesis. Each source type comes with different trade-offs. Galactic Center studies will be very sensitive to the assumed distribution of DM. The central DM density can vary substantially as demonstrated in Figure 2.12. At distances close to the center of the galaxy, or small r , the differences in DM densities can be 3-4 orders of magnitude. Searches toward the galactic center will therefore be quite sensitive to the assumed DM distribution.

Searches toward Dwarf Spheroidal Galaxies (dSph's) suffer from uncertainties in the DM density less than the galactic center studies. This is mostly from their diminutive size being smaller than the angular resolution of most γ -ray observatories [18]. The DM content dSph's are typically determined with the Virial theorem, Equation (2.1), and are usually majority DM [18] in mass. DSph's tend to be ideal sources to look at for DM searches. Their environments are quiet with little

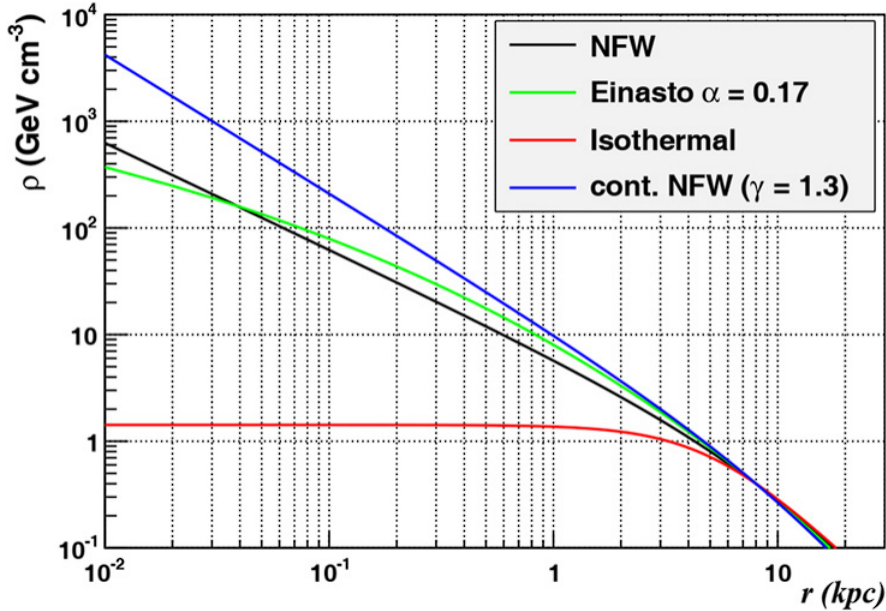


Figure 2.12 Different dark matter density profiles compared. Some models produce exceptionally large densities at small r [20].

470 astrophysical background. Unlike the galactic center, the most active components of dSph's are the
 471 stars within them versus a violent accretion disc around a black hole. All this together means that
 472 dSph's are among the best sources to look at for indirect DM searches. dSph's are the targets of
 473 focus for this thesis.

474 2.6 Multi-Messenger Dark Matter

475 Astrophysics entered a new phase in the past few decades that leverages our increasing sensitivity
 476 to SM channels and general relativity (GR). Up until the 21st century, astrophysical observations
 477 were performed with photons (γ) only. Astrophysics with this 'messenger' is fairly mature now.
 478 Novel observations of the universe have since only adjusted the sensitivity of the wavelength of
 479 light that is observed except at MeV energies. Gems like the CMB [10], and more have ultimately
 480 been observations of different wavelengths of light. Multi-messenger astrophysics proposes using
 481 other SM particles such the p^{+-} , or ν or gravitation waves predicted by general relativity.

482 The experiment LIGO had a revolutionary discovery in 2016 with the first detection of a binary
 483 black hole merger [21]. This opened the collective imagination to observing the universe through
 484 gravitational waves. There has also been a surge of interest in the neutrino (ν) sector. IceCube

485 demonstrated that we are sensitive to neutrinos in regions that correlate with significant photon
 486 emission like the galactic plane [22]. Neutrinos, like gravitational waves and light, travel mostly
 487 unimpeded from their source to our observatories. This makes pointing to the originating source
 488 of these messengers much easier than it is for cosmic rays which are deflected from their source by
 489 magnetic fields.

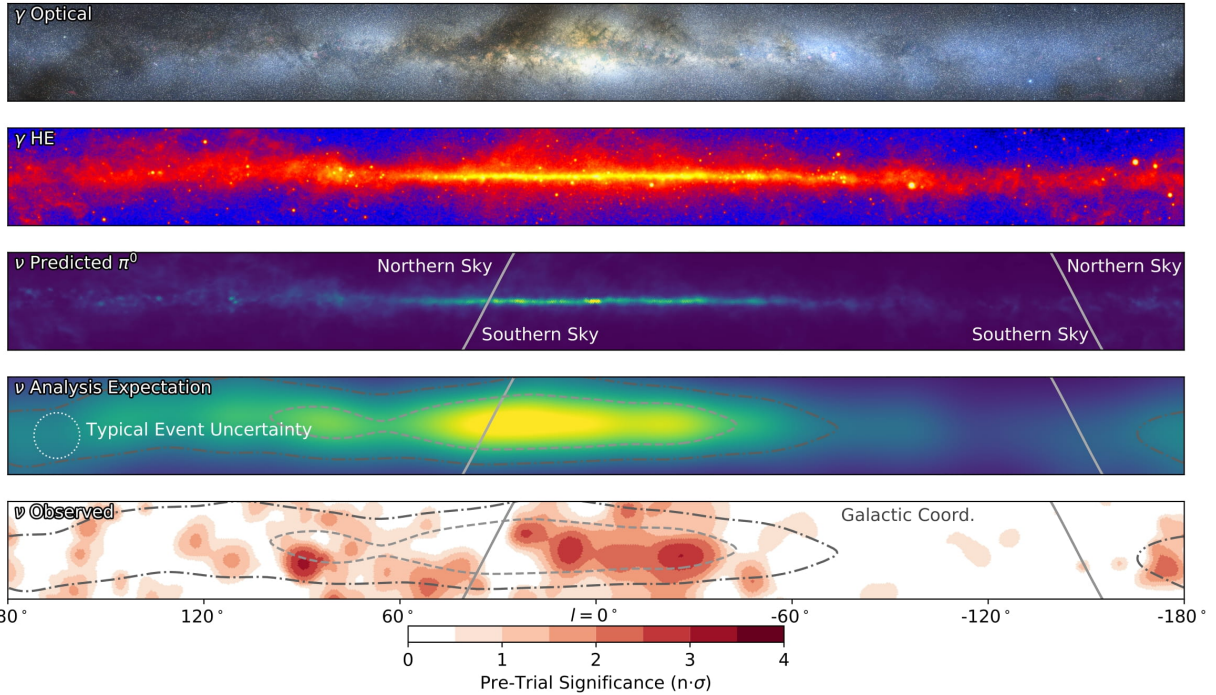


Figure 2.13 The Milky Way Galaxy in photons (γ) and neutrinos (ν) [22]. The Galactic center is at $l=0^\circ$ and is the brightest region in all panels. (top) An Optical color image of the Milky Way galaxy seen from Earth. Clouds of gas and dust obscure some light from stars. (2nd down) Integrated flux of γ -rays observed by the Fermi-LAT telescope [23]. (middle) Expected neutrino emission that corresponds with Fermi-LAT observations. (2nd up) Expected neutrino emission profile after considering detector systematics of IceCube. (bottom) Observed neutrino emission from region of the galactic plane. Substantial neutrino emission was detected.

490 The IceCube collaboration recently published a groundbreaking result of the Milky Way in
 491 neutrinos. The recent result from IceCube, shown in Figure 2.13, proves that we can make
 492 observations under different messenger regimes. The top two panels show the appearance of the
 493 galactic plane to different wavelengths of light. Some sources are more apparent in some panels,
 494 while others are not. This new channel is powerful because neutrinos are readily able to penetrate
 495 through gas and dust in the Milky Way. This new image also refines our understanding of how high

496 energy particles are produced. For example, the fit to IceCube data prefers neutrino production
 497 from the decay of π^0 [22].

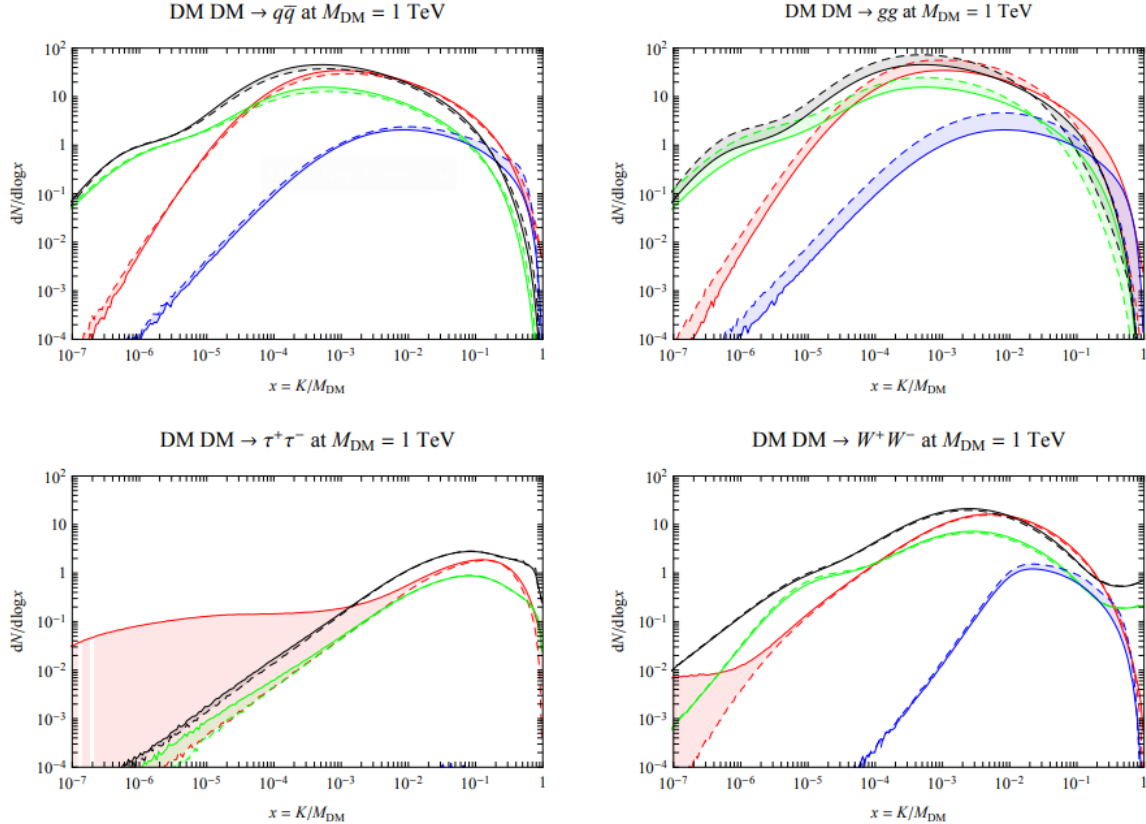


Figure 2.14 Dark Matter annihilation spectra for different final state particle and standard model annihilation channels [24]. Photons (red), e^\pm (green), \bar{p} (blue), ν (black).

498 Exposing our observations to more cosmic messengers greatly increases our sensitivity to
 499 rare processes. In the case of DM, Figure 2.14, there are many SM particles produced in DM
 500 annihilation. Among the final state fluxes are gammas and neutrinos. Charged particles are also
 501 produced however they would not likely make it to Earth since they will be deflected by magnetic
 502 fields between the source and Earth. This means observatories that can see the neutral messengers
 503 are especially good for DM searches and for combining data for a multi-messenger DM search.

CHAPTER 3

504 MULTIMESSENGER ASTROPHYSICS: DETECTING HIGH ENERGY NEUTRAL 505 MESSENGERS

506 3.1 Introduction

507 Before the 20th century, all asttrophysics observations were optical in nature. We litterly only
508 saw things with highly magnified optical observations. Then we discovered cosmic rays. cosmic
509 rays are charged particles, typically naked protons or H+. This was seen by Victor Hess in 19??.
510 Around the same time we discovered neutrinos from beta decay. Sometime around 1950 we started
511 to build neutrino detectors which were mostly sensitive to neutrinos from the sun. Finally, it was
512 theorized that compact objects like black holes and neutron stars would create waves in space-time
513 when they experience mergers or collisions.

514 In the 21st century, we have developed new observation techniques and detectors that are no only
515 sensitive to these four messengers - photons (TODO: photon), neutrinos (TODO: nu), Cosmic
516 Rays (CR), and Gravitational Wave (WV) - we're collect high energy versions of these events.
517 For the standad model particles, we're now sensitive to all messengers above the MeV eneryg
518 range. Additionally, the GW's were sensitive to are in the stellar mass black hole region and above
519 within our galactic neighborhood. This means were becoming sensitive to the fundamental physics
520 occuring within the universe and we can rely on the universe as a TeV+ particle accelerator. We
521 also have the abaility to correlate high energy events across messengers and gain new insights on
522 the processes that occur in our universe.

523 This thesis focuses on very high energy (VHE) gamma rays and neutrinos. These can both be
524 observed through the water cherenkov detection technique altho not exclusively. Methods on how
525 to detect and observe these neutral messengers are discussed Section 3.3 and Section 3.4

526 3.2 Charged Particles in a Medium

527 For high enery gamma-rays and neutrinos, we can exploit the same effect that charged particles
528 have with water. This effect is known as Cherenkov radiation. Cherenkov Radiation occurs when a
529 charged particle, usually electrons (e) or muons (μ), traverse a medium, like water, faster than the

530 speed of light in that medium. This is similar to sonic boom where an object moves through air
531 faster than the speed of sound in air. Cherenkov radiation can therefore be thought of as an 'optic
532 boom'. Many astro-particle physics experiments will use water as the medium as because water
533 has a unique set of properties ideal for charged particle tracking.



Figure 3.1 TODO: Show a nuclear reactor with cherenkov radiation[NEEDS A SOURCE][FACT CHECK THIS]

534 The frequency of light emitted due to cherenkov radiation follows the equation:

$$INSERT\ Cherenkov\ wavelength\ calc\ HERE. \quad (3.1)$$

535 The absorption spectra is shown in the following figure:

536 **3.3 Photons (γ)**

537 **3.4 Neutrinos (ν)**

538 **3.5 Opportunities to Combine for Dark Matter**



Figure 3.2 TODO: absorption spectrum of liquid and solid water[NEEDS A SOURCE][FACT CHECK THIS]

CHAPTER 4

539

HIGH ALTITUDE WATER CHERENKOV (HAWC) OBSERVATORY

540 **4.1 The Detector**

541 **4.2 Events Reconstruction and Data Acquisition**

542 **4.2.1 G/H Discrimination**

543 **4.2.2 Angle**

544 **4.2.3 Energy**

545 **4.3 Remote Monitoring**

546 **4.3.1 ATHENA Database**

547 **4.3.2 HOMER**

548

CHAPTER 5

ICECUBE NEUTRINO OBSERVATORY

549 **5.1 The Detector**

550 **5.2 Events Reconstruction and Data Acquisition**

551 **5.2.1 Angle**

552 **5.2.2 Energy**

553 **5.3 Northern Test Site**

554 **5.3.1 PIgeon remote dark rate testing**

555 **5.3.2 Bulkhead Construction**

CHAPTER 6

COMPUTATIONAL TECHNIQUES IN PARTICLE ASTROPHYSICS

557 **6.1 Neural Networks for Gamma/Hadron Separation**

558 **6.2 Parallel Computing for Dark Matter Analyses**

559

CHAPTER 7

GLORY DUCK

560 **7.1 Dataset and Background**561 **7.1.1 Data Files**

- 562 • Detector Resolution: `response_aerie_svn_27754_systematics_best_mc_test_no`
 563 `broadpulse_10pctlogchargesmearing_0.63qe_25kHzNoise_run5481_curvatu`
 564 `re0_index3.root`
- 565 • Data Map: `maps-20180119/liff/maptree_1024.root`

566 **7.1.2 Data Set Chosen**

567 The maps used for this analysis contain 1017 days of data between runs 2104 (2014-11-26) and
 568 7476 (2017-12-20). They were generated from pass 4.0 reconstruction. The analysis is performed
 569 using the f_{hit} energy binning scheme with bins [1-9] similar to what was done for the Crab and
 570 previous HAWC dSph analysis. [25, 26].

571 **7.1.3 Background Estimation**

572 This analysis was done on dwarf spheroidal (dSph) galaxies because of their large dark matter
 573 (DM) content relative to baryonic. We consider the following to estimate the background to this
 574 study.

- 575 • The dSphs are small in HAWC's field of view, so the analysis is not sensitive to large or small
 576 scale anisotropies.
- 577 • The dSphs used in this analysis are off the galactic plane.
- 578 • The dSphs are baryonically faint relative to their expected dark matter content and are not
 579 expected to contain gamma-ray sources.

580 Therefor we make no additional assumptions of the background coming from our sources and
 581 use HAWC's standard direct integration method for background estimation. It is possible for gamma

582 rays from DM annihilation to scatter in transit to HAWC via Inverse Compton Scattering (ICS).
583 This was investigated and its impact on the flux is basically zero. Supporting information on this
584 is in **TODO: refer to appdx**

585 **7.1.4 Software Tools and Development**

586 This analysis was performed using HAL and 3ML, in Python version 2.[25, 27] Dan developed
587 a source model to implement the *Poor Particle Physicists' Cookbook* (PPPC) [28] into HAWC
588 software. This model and corresponding Monte Carlo simulation was consolidated into a dictionary
589 for other collaborators. A NumPy version of this dictionary was made for both Py2 and Py3. The
590 code base for creating this dictionary is also in Dan's sandbox:

- 591 • Py2: <https://gitlab.com/hawc-observatory/sandboxes/salaza82/glory-duc>
592 k-hawc/-/tree/master/GD_spectrumDictionary Generator (Deprecated)
- 593 • Py3: <https://gitlab.com/hawc-observatory/sandboxes/salaza82/pppc2dict>
594 tPPPC2Dict

595 The analysis was performed using the f_{hit} framework performed in the Crab paper[25]. The
596 PPPC model selected for this analysis included electroweak corrections. Dictionaries for the
597 non-electroweak model were generated but not used for this analysis. The Python2 NumPy dictio-
598 nary file for gamma-ray final states is `dmCirSpecDict.npy`. The corresponding Python3 file is
599 `DM_CirrelliSpectrum_dict_gammas.npy`. These files can also be used for decay channels and
600 the PPPC describes how. [28]. Python's pickle is not backwards compatible, so scripts run in Py3
601 are not able to use dictionaries generated using Py2 and vice-versa.

602 All other software used for data analysis, DM profile generation, and job submission to SLURM
603 are also kept in my sandbox for <https://gitlab.com/hawc-observatory/sandboxes/sal>
604 aza82/glory-duck-hawc the Glory Duck project. They're broad descriptions are as follows:

- 605 • `GD_mass_profiles`: scripts that generate .fits maps for HAWC HAL according to [29].
606 Also contains simple plots of these maps.

- 607 • `GD_spectrum`: scripts that generate NumPy dictionaries of PPPC gamma spectra [28].
- 608 • `analysis_scripts`: HAL scripts for performing likelihood computation on HAWC data or
609 simulation with GD spectra and mass profiles.
- 610 • `pointing`: HAL scripts used to compare the impact of point systematic.
- 611 • `poisson_maps`: scripts for generating and managing poisson trials used for this study.

612 **7.2 Analysis**

613 **7.2.1 Monte Carlo Simulation**

614 The expected differential photon flux from a DM-DM annihilation to standard model particles
615 over solid angle is described by the familiar equation.

$$\frac{d\Phi_\gamma}{dE_\gamma} = \frac{\langle\sigma v\rangle}{8\pi m_\chi^2} \frac{dN_\gamma}{dE_\gamma} \times \int_{\text{source}} d\Omega \int_{l.o.s} \rho_\chi^2 dl(r, \theta') \quad (7.1)$$

616 here $\langle\sigma v\rangle$ is the velocity weighted annihilation cross-section. $\frac{dN}{dE}$ is the expected differential number
617 of photons produced at each energy per annihilation. M_χ is the rest mass of the supposed DM
618 particle. J is the astrophysical J-factor and is defined as

619 ρ_χ is the DM density. For this value, we import the PPPC with electroweak corrections [28].
620 The spectrum is implemented as a model script in astromodels for 3ML. The J-factor profiles for
621 each source is imported from Geringer-Sameth (\mathcal{GS}) [30]. Another DM distribution model from
622 Bonnivard (\mathcal{B}) [31] was used for the complete study. However, to save computational time, limits
623 from \mathcal{GS} were scaled to \mathcal{B} instead of each experiment performing a full study a second time. We
624 create NSIDE 16384 maps of the J-factors for each dSph. These maps are integrated over every
625 spatial bin and passed to the fitting software. Plots of these maps are provided for each source in
626 the sandbox directory: `GD_mass_profiles`.

627 **7.2.2 Source Selection and Annihilation Channels**

628 We use many of the dSph presented in our previous dSph DM search [26]. HAWC's sources
629 for Glory Duck include Boötes I, Coma Berenices, Canes Venatici I + II, Draco, Hercules, Leo I,

630 II, + IV, Segue 1, Sextans, and Ursa Major I + II. A full description of all sources used in Glory
 631 Duck is found in Table 7.1. Triangulum II was excluded from the Glory Duck analysis because
 632 of large uncertainties in its J-factor. Ursa Minor was excluded from HAWC’s contribution to the
 633 combination because the source extension model extended Ursa Minor beyond HAWC’s field of
 634 view. Ursa Minor was not expected to contribute significantly to the combined limit, so work was
 635 not invested in a solution to include Ursa Minor.

636 The DM annihilation channels probed for the Glory Duck combination include
 637 $b\bar{b}$, $e\bar{e}$, $\mu\bar{\mu}$, $\tau\bar{\tau}$, $t\bar{t}$, W^+W^- , and ZZ . A summary of all sources, with a description of each ex-
 638 periments’ sensitivity to the source, is provided in Table 7.2.

639 7.2.3 Likelihood Methods

640 We perform a standard HAWC binned maximum likelihood analysis using f_{hit} bins 1-9. This
 641 analysis was performed using HAL and 3ML, in Python2 [25, 27]. With these tools we compute
 642 the max from the likelihood profiles and perform a ratio test to calculate the significance of each
 643 source. This analysis is identical to the previous dSph analysis [26] except the sources are treated
 644 as extended. For the vast majority of our sources, this extension is no greater than 2 degrees. We
 645 calculate the likelihood of each source and model, assuming events are Poisson distributed, with

$$\mathcal{L} = \prod_i \frac{(B_i + S_i)^{N_i} e^{-(B_i + S_i)}}{N_i!} \quad (7.2)$$

646 S_i is the sum of expected number of signal counts. B_i is the number of background counts
 647 observed. N_i is the total number of counts. The i th bin is iterated over spatial and f_{hit} . Then we
 648 combine the profiles across all five experiments. The profile likelihood ratio λ as a function of
 649 annihilation cross-section $\langle\sigma v\rangle$ is computed by:

$$\lambda(\langle\sigma v\rangle | \mathcal{D}_{\text{dSphs}}) = \frac{\mathcal{L}(\langle\sigma v\rangle; \hat{\nu} | \mathcal{D}_{\text{dSphs}})}{\mathcal{L}(\widehat{\langle\sigma v\rangle}; \hat{\nu} | \mathcal{D}_{\text{dSphs}})} \quad (7.3)$$

650 for a considered annihilation channel and DM mass.

651 **TODO: Section pasted from paper. Rephrase cause plagiarism is a thing.** As mentioned pre-
 652 viously, each experiment computes the \mathcal{L}_{lk} from Equation (7.3) differently. The remainder of

Table 7.1 Summary of the relevant properties of the dSphs used in the present work. Column 1 lists the dSphs. Columns 2 and 3 present their heliocentric distance and galactic coordinates, respectively. Columns 4 and 5 report the J -factors of each source given from the \mathcal{GS} and \mathcal{B} independent studies and their estimated $\pm 1\sigma$ uncertainties. The values $\log_{10} J$ (\mathcal{GS} set) [30] correspond to the mean J -factor values for a source extension truncated at the outermost observed star. The values $\log_{10} J$ (\mathcal{B} set) [31] are provided for a source extension at the tidal radius of each dSph. **Bolded sources are within HAWC's field of view and provided to the Glory Duck analysis.**

Name	Distance (kpc)	l, b ($^{\circ}$)	$\log_{10} J$ (\mathcal{GS} set) $\log_{10}(\text{GeV}^2\text{cm}^{-5}\text{sr})$	$\log_{10} J$ (\mathcal{B} set) $\log_{10}(\text{GeV}^2\text{cm}^{-5}\text{sr})$
Boötes I	66	358.08, 69.62	$18.24^{+0.40}_{-0.37}$	$18.85^{+1.10}_{-0.61}$
Canes Venatici I	218	74.31, 79.82	$17.44^{+0.37}_{-0.28}$	$17.63^{+0.50}_{-0.20}$
Canes Venatici II	160	113.58, 82.70	$17.65^{+0.45}_{-0.43}$	$18.67^{+1.54}_{-0.97}$
Carina	105	260.11, -22.22	$17.92^{+0.19}_{-0.11}$	$18.02^{+0.36}_{-0.15}$
Coma Berenices	44	241.89, 83.61	$19.02^{+0.37}_{-0.41}$	$20.13^{+1.56}_{-1.08}$
Draco	76	86.37, 34.72	$19.05^{+0.22}_{-0.21}$	$19.42^{+0.92}_{-0.47}$
Fornax	147	237.10, -65.65	$17.84^{+0.11}_{-0.06}$	$17.85^{+0.11}_{-0.08}$
Hercules	132	28.73, 36.87	$16.86^{+0.74}_{-0.68}$	$17.70^{+1.08}_{-0.73}$
Leo I	254	225.99, 49.11	$17.84^{+0.20}_{-0.16}$	$17.93^{+0.65}_{-0.25}$
Leo II	233	220.17, 67.23	$17.97^{+0.20}_{-0.18}$	$18.11^{+0.71}_{-0.25}$
Leo IV	154	265.44, 56.51	$16.32^{+1.06}_{-1.70}$	$16.36^{+1.44}_{-1.65}$
Leo V	178	261.86, 58.54	$16.37^{+0.94}_{-0.87}$	$16.30^{+1.33}_{-1.16}$
Leo T	417	214.85, 43.66	$17.11^{+0.44}_{-0.39}$	$17.67^{+1.01}_{-0.56}$
Sculptor	86	287.53, -83.16	$18.57^{+0.07}_{-0.05}$	$18.63^{+0.14}_{-0.08}$
Segue I	23	220.48, 50.43	$19.36^{+0.32}_{-0.35}$	$17.52^{+2.54}_{-2.65}$
Segue II	35	149.43, -38.14	$16.21^{+1.06}_{-0.98}$	$19.50^{+1.82}_{-1.48}$
Sextans	86	243.50, 42.27	$17.92^{+0.35}_{-0.29}$	$18.04^{+0.50}_{-0.28}$
Ursa Major I	97	159.43, 54.41	$17.87^{+0.56}_{-0.33}$	$18.84^{+0.97}_{-0.43}$
Ursa Major II	32	152.46, 37.44	$19.42^{+0.44}_{-0.42}$	$20.60^{+1.46}_{-0.95}$
Ursa Minor	76	104.97, 44.80	$18.95^{+0.26}_{-0.18}$	$19.08^{+0.21}_{-0.13}$

Table 7.2 Summary of dSph observations by each experiment used in this work. A ‘-’ indicates the experiment did not observe the dSph for this study. For Fermi-LAT, the exposure at 1 GeV is given. For HAWC, $|\Delta\theta|$ is the absolute difference between the source declination and HAWC latitude. HAWC is more sensitive to sources with smaller $|\Delta\theta|$. For IACTs, we show the zenith angle range, the total exposure, the energy range, the angular radius θ of the signal or ON region, the ratio of exposures between the background-control (OFF) and signal (ON) regions (τ), and the significance of gamma-ray excess in standard deviations, σ .

Source name	Fermi-LAT	HAWC	H.E.S.S, MAGIC, VERITAS						
	Exposure (10^{11} s m 2)	$ \Delta\theta $ (°)	IACT	Zenith (°)	Exposure (h)	Energy range (GeV)	θ (°)	τ	S (σ)
Boötes I	2.6	4.5	VERITAS	15 – 30	14.0	100–41000	0.10	8.6	-1.0
Canes Venatici I	2.9	14.6	–	–	–	–	–	–	–
Canes Venatici II	2.9	15.3	–	–	–	–	–	–	–
Carina	3.1	–	H.E.S.S.	27 – 46	23.7	310 – 70000	0.10	18.0	-0.3
Coma Berenices	2.7	4.9	H.E.S.S.	47 – 49	11.4	550 – 70000	0.10	14.4	-0.4
Draco	3.8	38.1	MAGIC	5 – 37	49.5	60 – 10000	0.17	1.0	–
			MAGIC	29 – 45	52.1	70 – 10000	0.22	1.0	–
			VERITAS	25 – 40	49.8	120 – 70000	0.10	9.0	-1.0
Fornax	2.7	–	H.E.S.S.	11 – 25	6.8	230 – 70000	0.10	45.5	-1.5
Hercules	2.8	6.3	–	–	–	–	–	–	–
Leo I	2.5	6.7	–	–	–	–	–	–	–
Leo II	2.6	3.1	–	–	–	–	–	–	–
Leo IV	2.4	19.5	–	–	–	–	–	–	–
Leo V	2.4	–	–	–	–	–	–	–	–
Leo T	2.6	–	–	–	–	–	–	–	–
Sculptor	2.7	–	H.E.S.S.	10 – 46	11.8	200 – 70000	0.10	19.8	-2.2
Segue I	2.5	2.9	MAGIC	13 – 37	158.0	60 – 10000	0.12	1.0	-0.5
			VERITAS	15 – 35	92.0	80 – 50000	0.10	7.6	0.7
Segue II	2.7	–	–	–	–	–	–	–	–
Sextans	2.4	20.6	–	–	–	–	–	–	–
Ursa Major I	3.4	32.9	–	–	–	–	–	–	–
Ursa Major II	4.0	44.1	MAGIC	35 – 45	94.8	120 – 10000	0.30	1.0	-2.1
Ursa Minor	4.1	–	VERITAS	35 – 45	60.4	160 – 93000	0.10	8.4	-0.1

653 this section highlights the differences in this calculation across the experiments. Four experiments,
 654 namely *Fermi*-LAT, H.E.S.S., HAWC and MAGIC, use a binned likelihood to compute the \mathcal{L}_{lk} . For
 655 these experiments, for each observation \mathcal{D}_{lk} of a given dSph l carried out using a given gamma-ray
 656 detector k , the binned likelihood function is:

$$\mathcal{L}_{lk}(\langle\sigma v\rangle; J_l, \nu_{lk} | \mathcal{D}_{lk}) = \prod_{i=1}^{N_E} \prod_{j=1}^{N_P} \left[\mathcal{P}(s_{lk,ij}(\langle\sigma v\rangle, J_l, \nu_{lk}) + b_{lk,ij}(\nu_{lk} | N_{lk,ij})) \right] \times \mathcal{L}_{lk,\nu}(\nu_{lk} | \mathcal{D}_{\nu_{lk}}) \quad (7.4)$$

658 where N_E and N_P are the number of considered bins in reconstructed energy and arrival
 659 direction, respectively; \mathcal{P} represents a Poisson PDF for the number of gamma-ray candidate events
 660 $N_{lk,ij}$ observed in the i -th bin in energy and j -th bin in arrival direction, when the expected number
 661 is the sum of the expected mean number of signal events s_{ij} (produced by DM annihilation) and of
 662 background events b_{ij} ; $\mathcal{L}_{lk,\nu}$ is the likelihood term for the extra ν_{lk} nuisance parameters that vary
 663 from one instrument k to another. The expected counts for signal events s_{ij} for a given dSph l and
 664 detector k is given by:

$$s_{ij}(\langle\sigma v\rangle, J) = \int_{E'_{\min,i}}^{E'_{\max,i}} dE' \int_{P'_{\min,j}}^{P'_{\max,j}} d\Omega' \int_0^\infty dE \int_{\Delta\Omega_{tot}} d\Omega \int_0^{T_{\text{obs}}} dt \frac{d^2\Phi(\langle\sigma v\rangle, J)}{dEd\Omega} \text{IRF}(E', P' | E, P, t) \quad (7.5)$$

665 where E' and E are the reconstructed and true energies, P' and P the reconstructed and true
 666 arrival directions; $E'_{\min,i}$, $P'_{\min,j}$, $E'_{\max,i}$, and $P'_{\max,j}$ are their lower and upper limits of the i -th
 667 energy bin and the j -th arrival direction bin; T_{obs} is the (dead-time corrected) total observation
 668 time; t is the time along the observations; $d^2\Phi/dEd\Omega$ is the DM flux in the source region (see
 669 Equation (7.1)); and $\text{IRF}(E', P' | E, P, t)$ is the IRF, which can be factorized as the product of the
 670 effective collection area of the detector $A_{\text{eff}}(E, P, t)$, the PDFs for the energy estimator $f_E(E' | E, t)$,
 671 and arrival direction $f_P(P' | E, P, t)$ estimators. Note that for *Fermi*-LAT, HAWC, MAGIC, and
 672 VERITAS the effect of the finite angular resolution is taken into account through the convolution
 673 of $d\Phi/dEd\Omega$ with f_P in Equation (7.5), whereas in the cases of H.E.S.S. f_P is approximated by a
 674 delta function. This approximation has been made in order to maintain compatibility of the result
 675 with what has been previously published. The difference introduced by this approximation is $< 5\%$

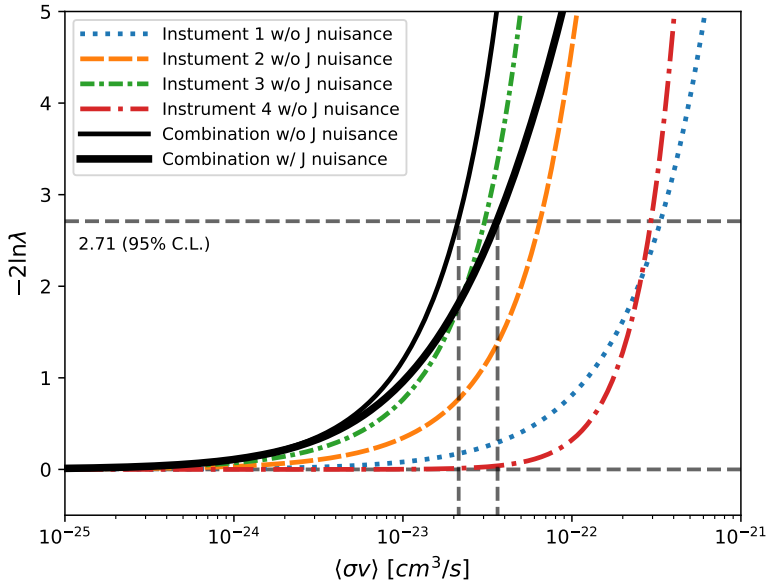


Figure 7.1 Illustration of the combination technique showing a comparison between $-2 \ln \lambda$ provided by four instruments (colored lines) from the observation of the same dSph without any J nuisance and their sum, *i.e.* the resulting combined likelihood (thin black line). According to the test statistics of Equation (7.6), the intersection of the likelihood profiles with the line $-2 \ln \lambda = 2.71$ indicates the 95% C.L. upper limit on $\langle \sigma v \rangle$. The combined likelihood (thin black line) shows a smaller value of upper limit on $\langle \sigma v \rangle$ than those derived by individual instruments. We also show the uncertainties on the J -factor affects the combined likelihood and degrade the upper limit on $\langle \sigma v \rangle$ (thick black line). All likelihood profiles are normalized so that the global minimum $\widehat{\langle \sigma v \rangle}$ is 0. We note that each profile depends on the observational conditions in which a target object was observed. The sensitivity of a given instrument can be degraded and the upper limits less constraining if the observations are performed in non optimal conditions such as a high zenith angle or a short exposure time.

676 for all considered dSphs. **TODO: End of paper section**

677 From Equation (7.3), we can compute the test statistic (TS) with the ratio test:

$$TS = -2 \ln \left(\frac{\mathcal{L}}{\mathcal{L}^{\max}} \right). \quad (7.6)$$

678 \mathcal{L}^{\max} here is equivalent to $\mathcal{L}(N_i, B_i, S_i = 0)$ or no signal counts.

679 7.3 HAWC Results

680 13 of the 20 dSphs considered for the Glory Duck analysis are within HAWC's field of view.

681 These dSph are analyzed for DM content according to the likelihood method described in Sec-

682 tion 7.2.3. The 13 likelihood profiles are then combined to create a combined limit on the dark
683 matter cross-section. This combination is done for 7 of the 8 annihilation channels used in the Glory
684 Duck analysis. Figure 7.2 shows the combined limit for all annihilation channels with HAWC only
685 observations. We also perform 300 studies of Poisson trials on the background. These trials are
686 used to produce HAWC Brazil bands are shared with the other collaborators for combined Brazil
687 Bands. The results on fitting to HAWC’s poisson trials of the DM hypothesis is shown in Figure 7.3
688 for seven of the DM annihilation channels.

689 No DM was found in HAWC observations. The limits are dominated by the dSph Segue1 and
690 Coma Berenices. The remaining 11 dSphs do no contribute significantly to the limit. Even though
691 the remaining dSphs have large J-factors, they are towards the edge of HAWC’s field of view where
692 this analysis is less sensitive.

693 **7.4 Glory Duck Combined Results**

694 The crux of this analysis is that HAWC’s results are combined with 4 other gamma-ray obser-
695 vatories: Fermi-LAT, H.E.S.S., MAGIC, and VERITAS. The complete joint likelihood for the l -th
696 dSph is the product of likelihood functions of the 5 experiments.

697 **TODO: place holder for results**

698 No significant DM emission was observed by any of the five telescopes. We present upper
699 limits on $\langle\sigma v\rangle$ using the test statistics, Eq. (7.6).

$$TS = -2 \ln \lambda(\langle\sigma v\rangle), \quad (7.7)$$

700 No significant DM emission was observed by any of the five instruments. We present the upper
701 limits on $\langle\sigma v\rangle$ assuming seven independent DM self annihilation channels, namely W^+W^- , Z^+Z^- ,
702 $b\bar{b}$, $t\bar{t}$, e^+e^- , $\mu^+\mu^-$, and $\tau^+\tau^-$. The 68% and 95% containment bands are produced from 300
703 Poisson realizations of the null hypothesis corresponding to each of the combined datasets. These
704 300 realizations are combined identically to dSph observations. The containment bands and the
705 median are extracted from the distribution of resulting limits on the null hypothesis. These 300
706 realizations are obtained either by fast simulations of the OFF observations, for H.E.S.S., MAGIC,

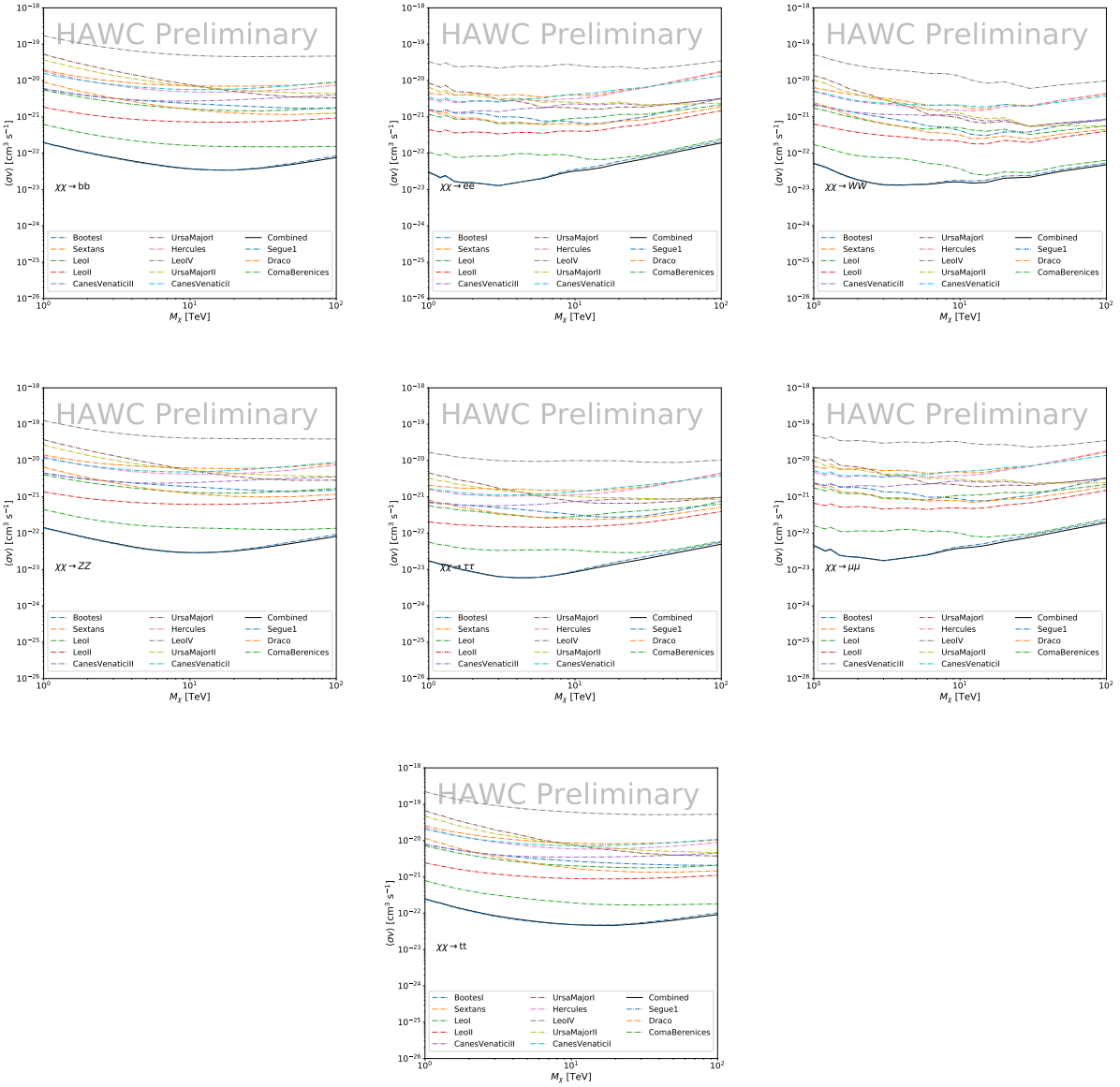


Figure 7.2 HAWC upper limits at 95% confidence level on $\langle\sigma v\rangle$ versus DM mass for seven annihilation channels, using the set of J -factors from Ref. [29]. The solid line represents the observed combined limit. Dashed lines represent limits from individual dSphs.

707 VERITAS, and HAWC, or taken from real observations of empty fields of view in the case of
 708 Fermi-LAT [32, 33, 34].

709 The obtained limits are shown in Figure 7.4 for the $\mathcal{G}\mathcal{S}$ set of J -factors [29] and in Figure 7.5
 710 for the \mathcal{B} set of J -factors [31, 35]. The combined limits are presented with their 68% and 95%
 711 containment bands, and are expected to be close to the median limit when no signal is present.

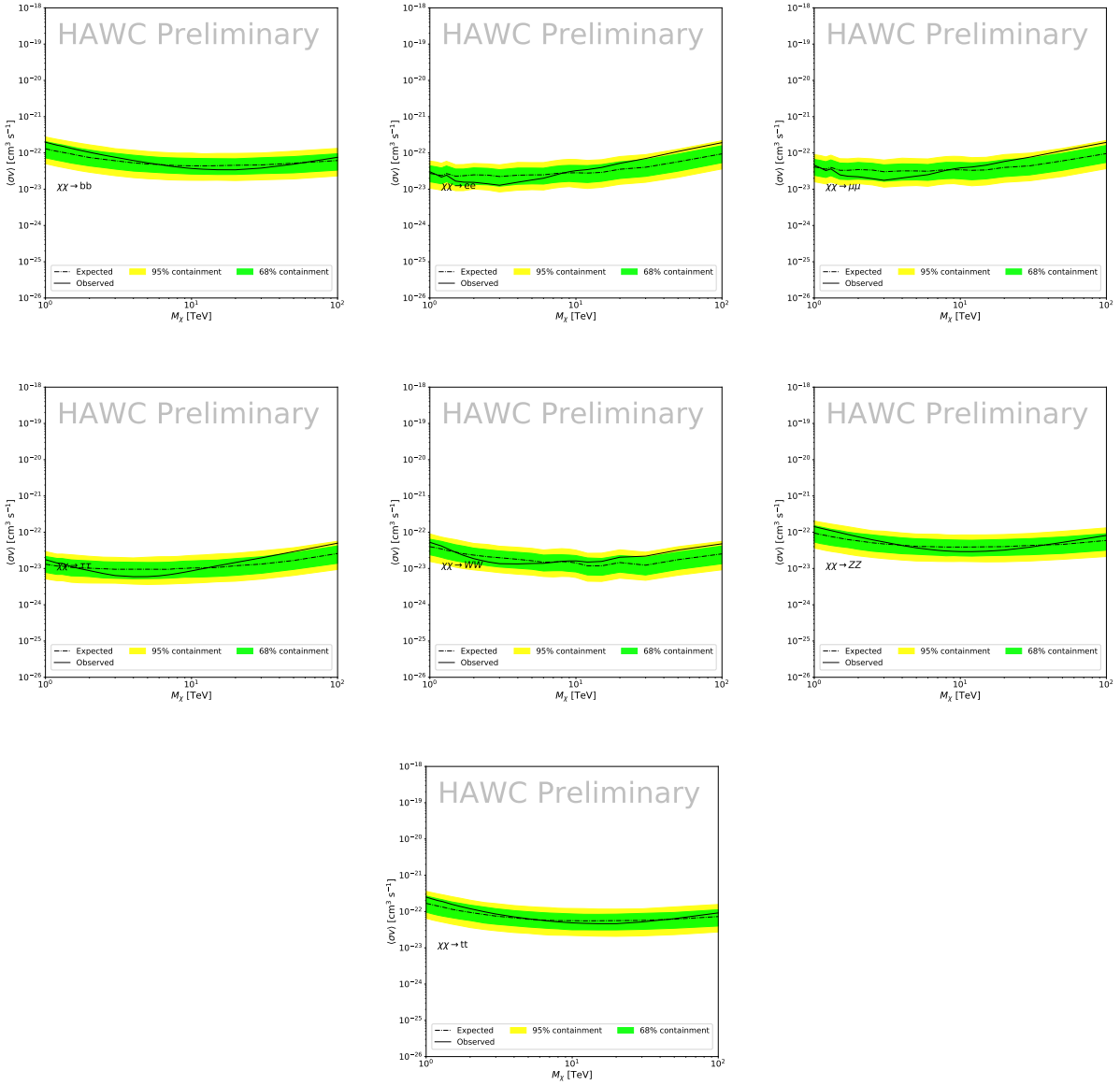


Figure 7.3 HAWC Brazil bands at 95% confidence level on $\langle\sigma v\rangle$ versus DM mass for seven annihilation channels with J -factors from \mathcal{GS} [29]. The solid line represents the combined limit from 13 dSphs. The dashed line is the expected limit. The green band is the 68% containment. The yellow band is the 95% containment.

712 We observe agreement with the null hypothesis for all channels, within 2σ standard deviations,
 713 between the observed limits and the expectations given by the median limits. Limits obtained from
 714 each detector are also indicated in the figures, where limits for all dSphs observed by the specific
 715 instrument have been combined.

716 Below ~ 300 GeV, the *Fermi*-LAT dominates the DM limits for all annihilation channels. From

717 ~ 300 GeV to ~ 2 TeV, *Fermi*-LAT continues to dominate for the hadronic and bosonic DM channels,
718 yet the IACTs (H.E.S.S., MAGIC, and VERITAS) and *Fermi*-LAT all contribute to the limit for
719 leptonic DM channels. For DM masses between ~ 2 TeV to ~ 10 TeV, the IACTs dominate leptonic
720 DM annihilation channels, whereas both the *Fermi*-LAT and the IACTs dominate bosonic and
721 hadronic DM annihilation channels. From ~ 10 TeV to ~ 100 TeV, both the IACTs and HAWC
722 contribute significantly to the leptonic DM limit. For hadronic and bosonic DM, the IACTs and
723 *Fermi*-LAT both contribute strongly.

724 We notice that the limits computed using the \mathcal{B} set of J -factor are always better compared to the
725 ones calculated with the \mathcal{GS} set. For the W^+W^- , Z^+Z^- , $b\bar{b}$, and $t\bar{t}$ channels, the ratio between the
726 limits computed with the two sets of J -factor is varying between a factor of ~ 3 and ~ 5 depending
727 on the energy, with the largest ratio around 10 TeV. For the channels e^+e^- , $\mu^+\mu^-$, and $\tau^+\tau^-$, the
728 ratio lies between ~ 2 to ~ 6 , being maximum around 1 TeV. Examining Figure 7.10 and Figure 7.11
729 in Section 7.6, these differences are explained by the fact that the \mathcal{B} set provides higher J -factors
730 for the majority of the studied dSphs, with the notable exception of Segue I. The variation on the
731 ratio of the limits for the two sets is due to different dSph dominating the limits depending on the
732 energy. This pushes the range of thermal cross-section which can be excluded to higher mass. This
733 comparison demonstrates the magnitude of systematic uncertainties associated with the choice of
734 the J -factor

735 This comparison demonstrates the magnitude of systematic uncertainties associated with the
736 choice of the J -factor calculation. The \mathcal{GS} and \mathcal{B} sets present a difference in the limits for all
737 channels of about This difference is explained, see Figure 7.10 and Figure 7.11 in Appendix, by the
738 fact that the \mathcal{B} set provides higher J factors for all dSph except for Segue I. This pushes the range
739 of thermal cross-section which can be excluded to higher mass.

740 7.5 Appendix: HAWC Systematics

741 7.5.1 Inverse Compton Scattering

742 The DM-DM annihilation channels produce many high energy electrons regardless of the
743 primary annihilation channel. These high energy electrons can produce high energy gamma-rays

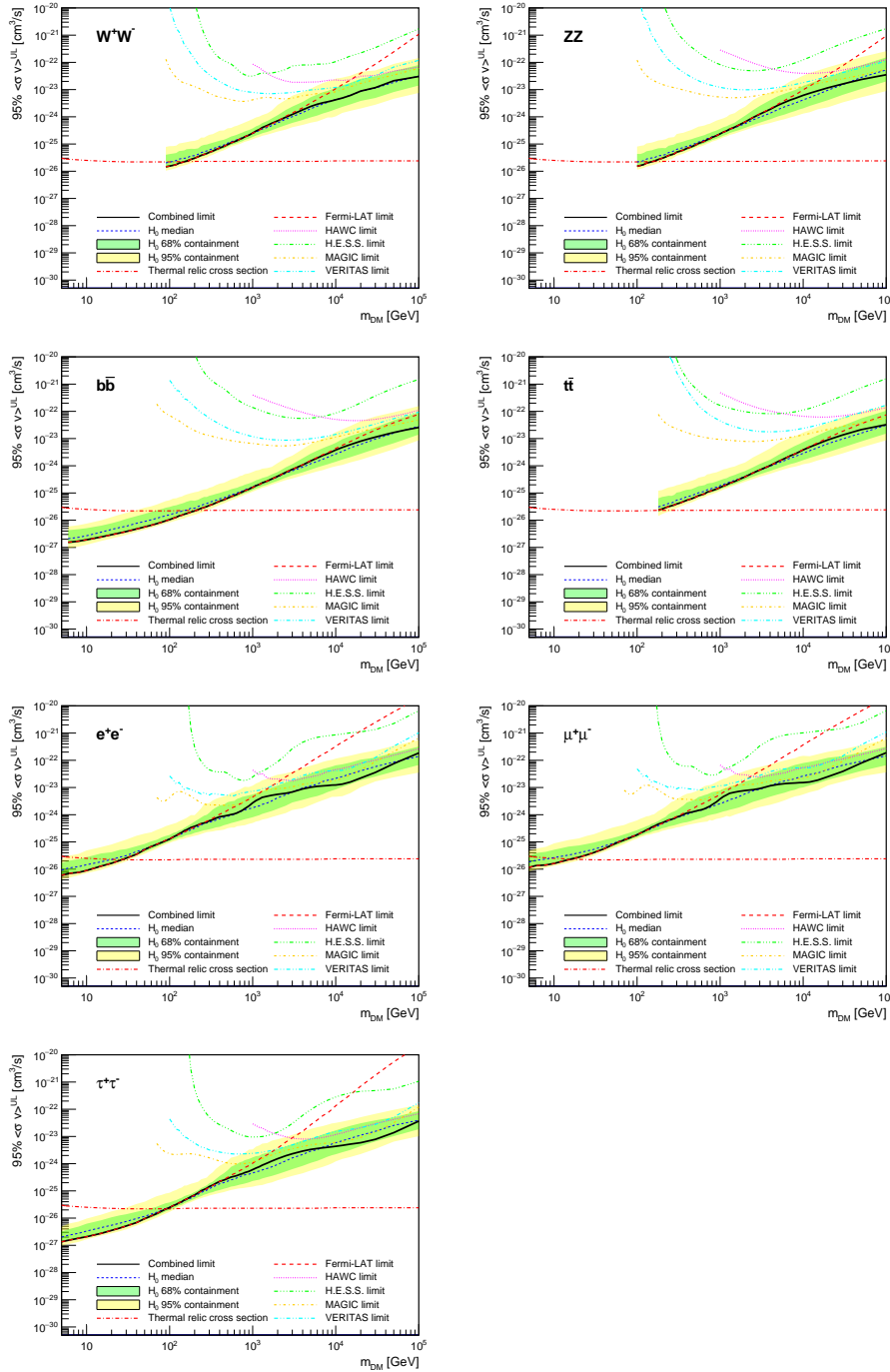


Figure 7.4 Upper limits at 95% confidence level on $\langle\sigma v\rangle$ in function of the DM mass for eight annihilation channels, using the set of J factors from Ref. [29] (\mathcal{GS} set in Table 7.1). The black solid line represents the observed combined limit, the black dashed line is the median of the null hypothesis corresponding to the expected limit, while the green and yellow bands show the 68% and 95% containment bands. Combined upper limits for each individual detector are also indicated as solid, colored lines. The value of the thermal relic cross-section in function of the DM mass is given as the red dotted-dashed line [36].

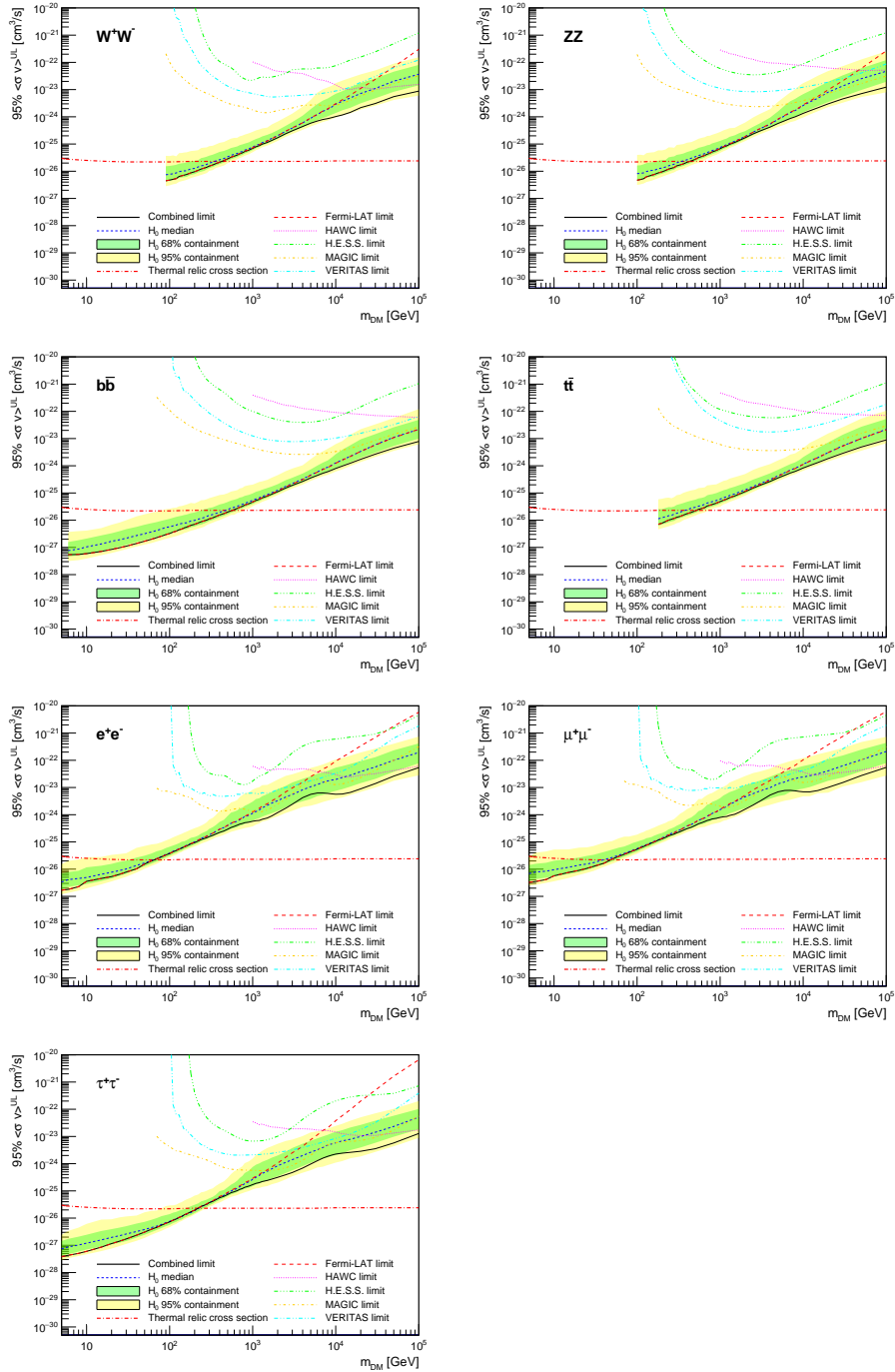


Figure 7.5 Same as Fig. 7.4, using the set of J factors from Ref. [31, 35] (\mathcal{B} set in Table 7.1).

through Inverse Compton Scattering (ICS). If this effect is strong, it would change the morphology of the source and increase the total expected gamma-ray counts from any source. The PPPC [28] provides tools in Mathematica for calculating the impact of ICS for an arbitrary location in the sky for a specified annihilation channel. We calculated the change in gamma-ray counts for DM

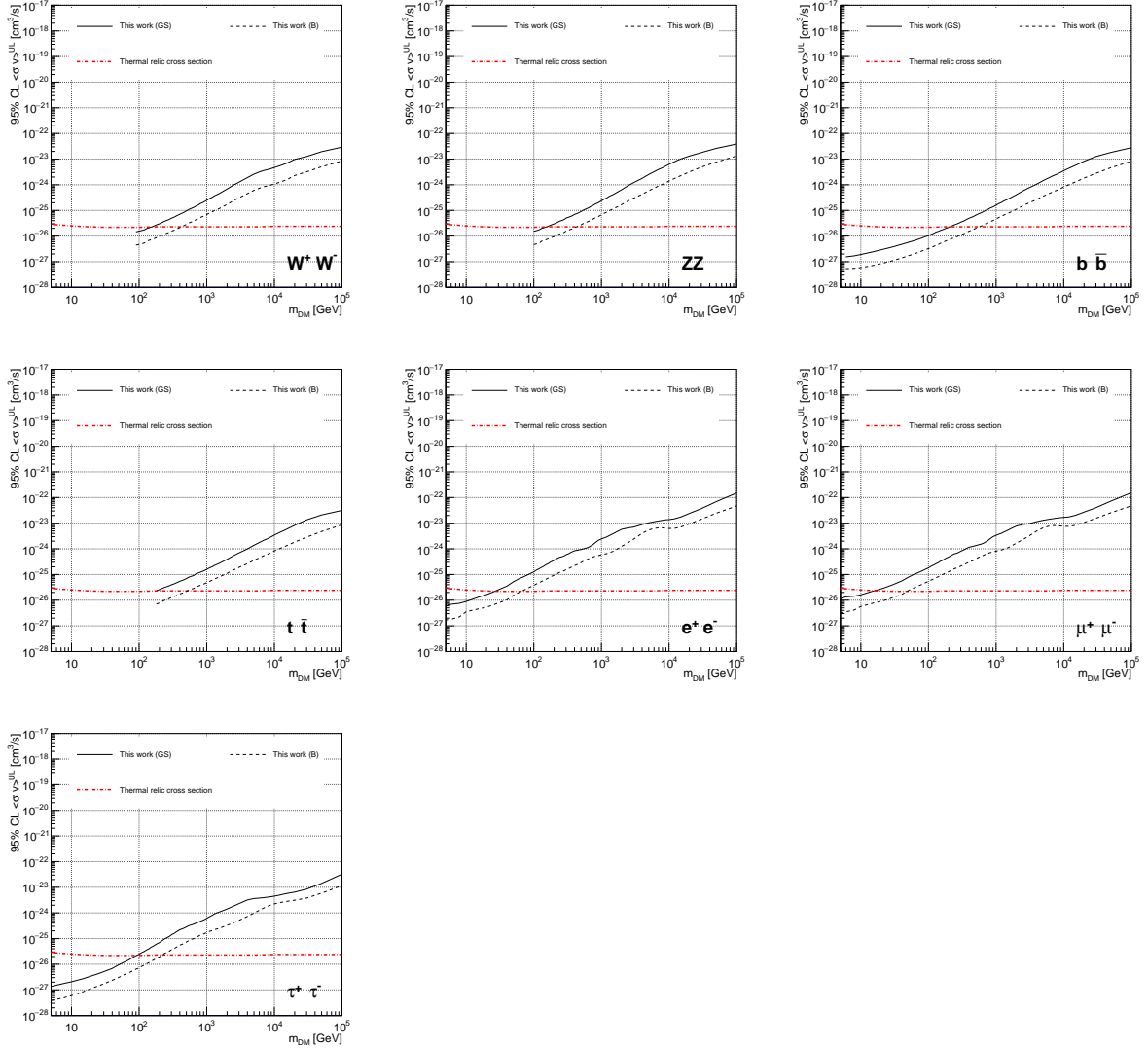


Figure 7.6 Comparisons of the combined limits at 95% confidence level for each of the eight annihilation channels when using the J factors from Ref. [29] (\mathcal{GS} set in Table 7.1), plain lines, and the J factor from Ref. [31, 35] (\mathcal{B} set in Table 7.1), dashed lines. The cross-section given by the thermal relic is also indicated [36].

748 annihilation to primary $e\bar{e}$ for RA and Dec corresponding to Segue1 and Coma Berenices. These
 749 dSphs were chosen because they are the strongest contributors to the limit. $e\bar{e}$ was selected because
 750 it would have the largest number of high energy electrons. The effect was found to be on the order
 751 of 10^{-7} on the gamma-ray spectrum. As a result, this systematic is not considered in our analysis.

752 7.5.2 Point Source Versus Extended Source Limits

753 The previous DM search toward dSph approximated the dSphs as point sources [26]. In
 754 this analysis, the dSphs are implemented as extended with J-factor distributions following those
 755 produced by [29]. The resolution of the cited map is much finer than HAWC's angular resolution.
 756 The vast majority of the J-factor distribution is represented on the central HAWC pixel of the dSph
 757 spatial map. However, the neighboring 8 pixels are not negligible and contribute to our limit.

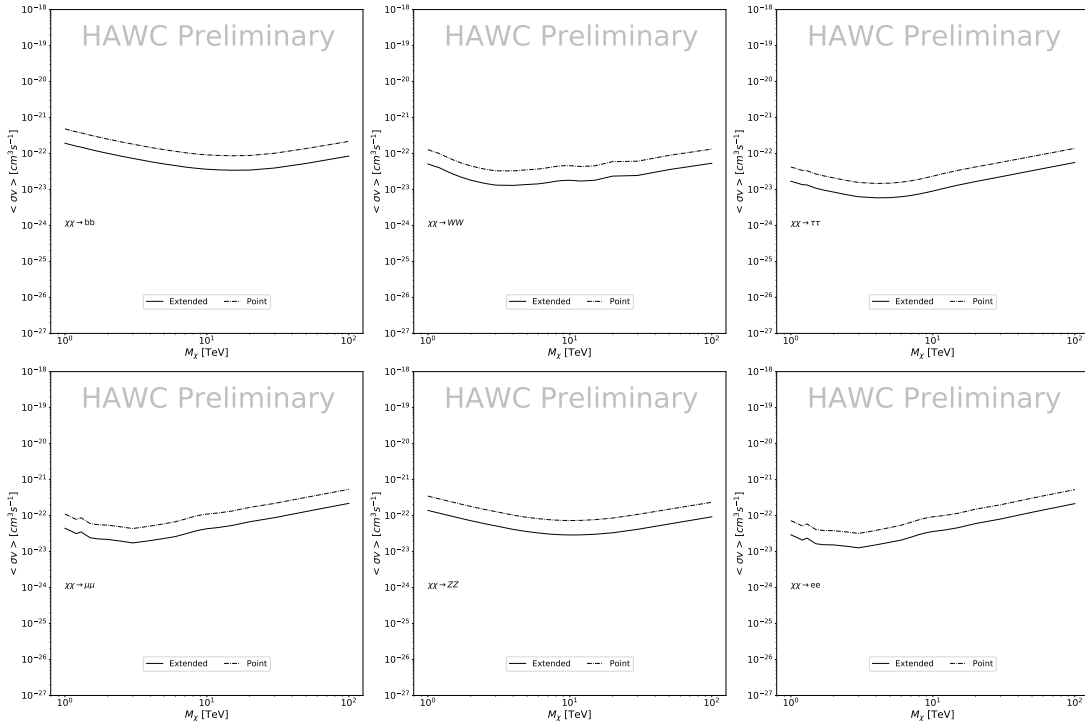


Figure 7.7 Comparisons of the combined limits at 95% confidence level for a point source analysis and extended source using [29] \mathcal{GS} J-factor distributions and PPPC [28] annihilation spectra. Shown are the limits for Segue1 which will have the most significant impact on the combined limit. 6 of the 7 DM annihilation channels are shown. Solid lines are extended source studies. Dashed lines are point source studies. Overall, the extended source analysis improves the limit by a factor of 2.

758 Figure 7.7 shows a substantial improvement to the limit for Segue1. Fig. 7.8 however showed
 759 identical limits. These disparities are best explained by the relative difference in their J-Factors.
 760 Both dSphs pass almost overhead the HAWC detector, however Segue1 has the larger J-Factor
 761 between the two. Adjacent pixels to the central pixel will therefore contribute to the limits. This is
 762 the case for other dSph that are closer to overhead the HAWC detector.

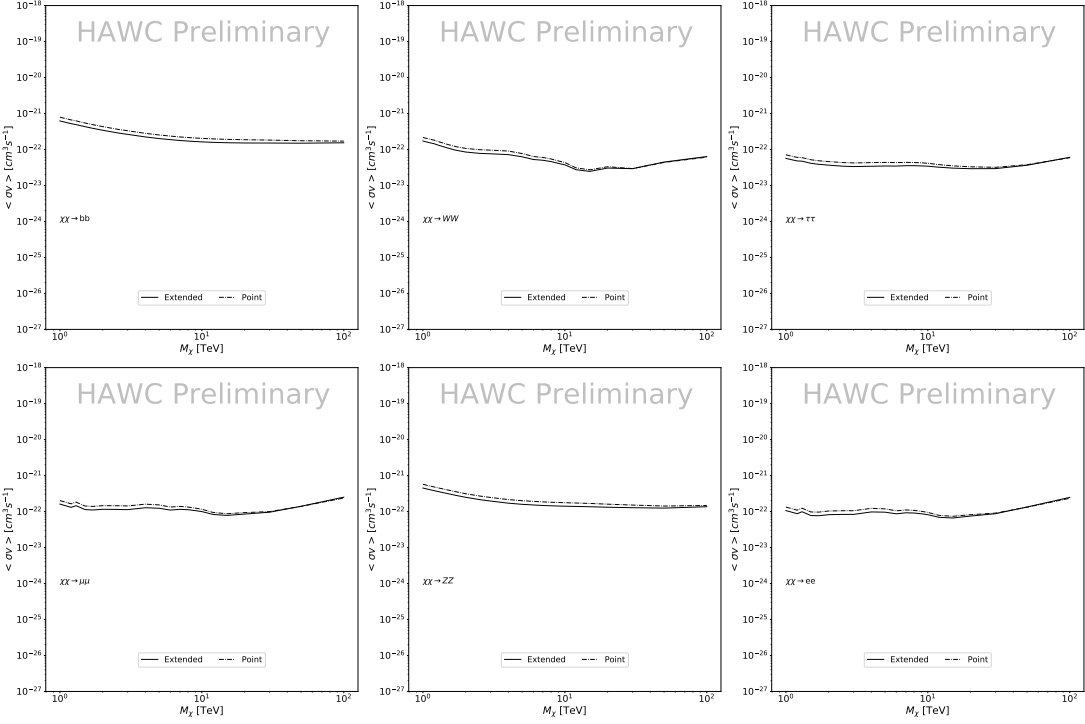


Figure 7.8 Same as Fig. 7.7 on Coma Berenices. This dSph also contributes significantly to the limit. The limits are identical in this case.

763 Comparison plots for all sources and the combined limit can be found in the sandbox for the
 764 Glory Duck project.

765 7.5.3 Impact of Pointing Systematic

766 During the analysis it was discovered that reconstruction of gamma-rays. Slides describing this
 767 systematic can be found here. Shown on the presentation is dependence on the pointing systematic
 768 on declination. New spatial profiles were generated for every dSph and limits were computed for
 769 the adjusted declination.

770 Section 7.5.3 demonstrates the impact of this systematic for all DM annihilation channels
 771 studied by HAWC. The impact is a tiny improvement, yet mostly identical, to the combined limits.

772 7.6 J-factor distributions

773 We show in this appendix a comparison between the J -factors computed by Geringer-Sameth
 774 *et al.* [29] (the \mathcal{GS} set) and the ones computed by Bonnivard *et al.* [31, 35] (the \mathcal{B} set). The
 775 \mathcal{GS} J -factors are computed through a Jeans analysis of the kinematic stellar data of the selected

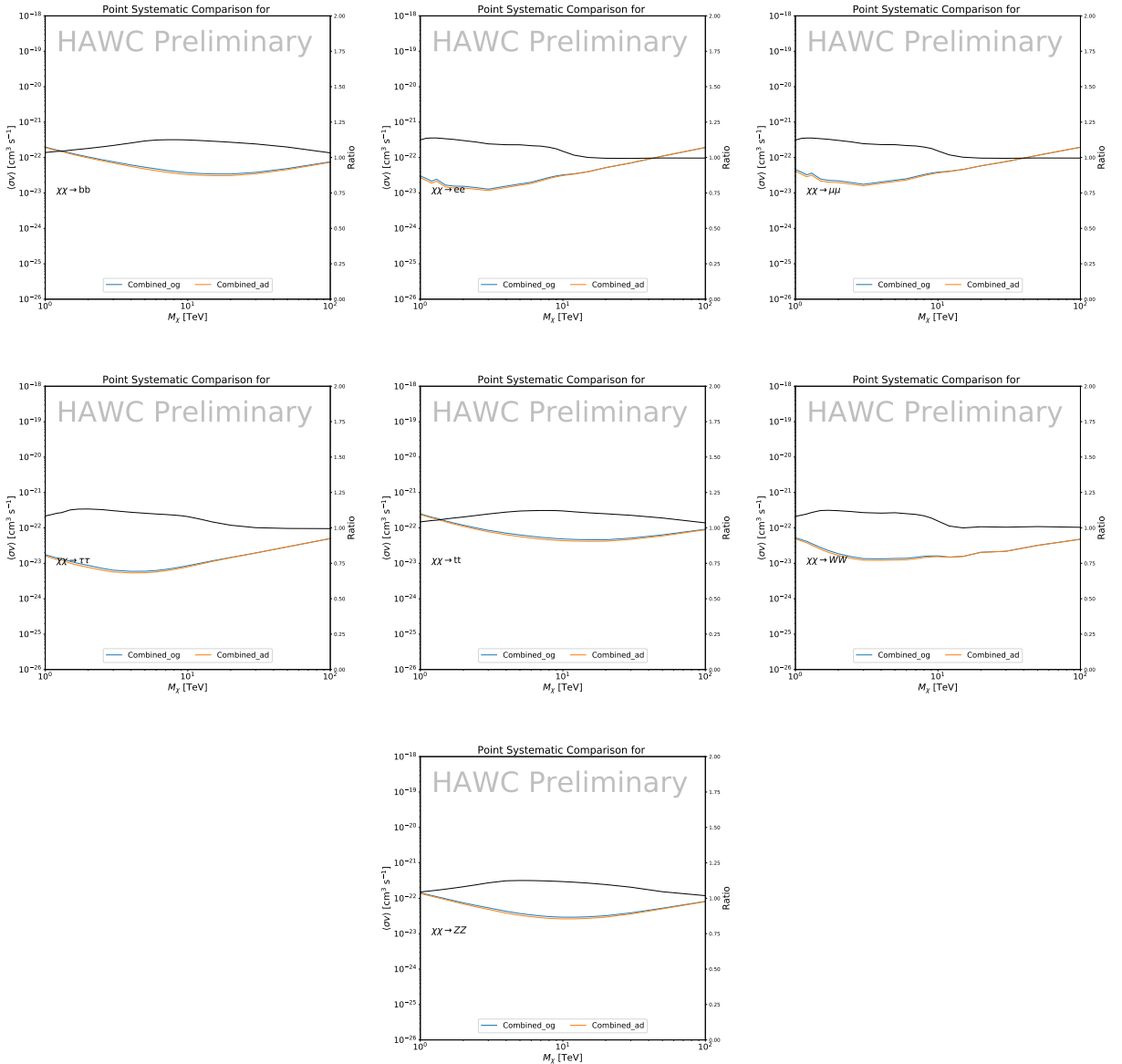


Figure 7.9 Comparison of combined limits when correcting for HAWC’s pointing systematic. All DM annihilation channels are shown. The solid black line is the ratio between published limit to the declination corrected limit. The blue solid line or “Combined_og” represented the limits computed for Glory Duck. The solid orange line or “Combined_ad” represented the limits computed after correcting for the pointing systematic.

776 dSphs, assuming a dynamic equilibrium and a spherical symmetry for the dSphs. They adopted
 777 the generalized DM density distribution, known as Zhao-Hernquist, introduced by [37], carrying
 778 three additional index parameters to describe the inner and outer slopes, and the break of the
 779 density profile. Such a profile parametrization allows the reduction of the theoretical bias from

780 the choice of a specific radial dependency on the kinematic data. In other words, the increase of
781 free parameters with the use of the Zhao-Hernquist profile allows a better description of the mass
782 density distribution of dark matter.

783 In addition, a constant velocity anisotropy profile and a Plummer light profile [38] for the stellar
784 distribution were assumed. The velocity anisotropy profile depends on the radial and tangential
785 velocity dispersions. However, its determination remains challenging since only the line-of-sight
786 velocity dispersion can be derived from velocity measurements. Therefore, the parametrization of
787 the anisotropy profile is obtained from simulated halos (see [39] for more details). They provide the
788 values of the J -factors of regions extending to various angular radius up to the outermost member
789 star.

790 The \mathcal{B} J -factors were computed through a Jeans analysis taking into account the systematic
791 uncertainties induced by the DM profile parametrization, the radial velocity anisotropy profile, and
792 the triaxiality of the halo of the dwarf galaxies. They performed a more complete study of the dSph
793 kinematics and dynamics than \mathcal{GS} for the determination of the J -factor. Conservative values of the
794 J -factors where obtained using an Einasto DM density profile [40], a realistic anisotropy profile
795 known as the Baes & Van Hese profile [41] which takes into account that the inner regions can be
796 significantly non-isotropic, and a Zhao-Hernquist light profile [37].

797 For both sets, J -factor values are provided for all dSphs as a function of the radius of the
798 integration region [29, 31, 35]. Table 7.1 shows the heliocentric distance and Galactic coordinates
799 of the twenty dSphs, together with the two sets of J -factor values integrated up to the outermost
800 observed star for \mathcal{GS} and the tidal radius for \mathcal{B} . Both J -factor sets were derived through a Jeans
801 analysis based on the same kinematic data, except for Draco where the measurements of [42] have
802 been adopted in the computation of the \mathcal{B} value. The computations for producing the \mathcal{GS} and \mathcal{B}
803 samples differ in the choice of the DM density, velocity anisotropy, and light profiles, for which the
804 set \mathcal{B} takes into account some sources of systematic uncertainties.

805 Figure 7.10 and Figure 7.11 show the comparisons for the J -factor versus the angular radius
806 for each of the 20 dSphs used in this study. The uncertainties provided by the authors are also

807 indicated in the figures. For the \mathcal{GS} set, the computation stops at the angular radius corresponding
 808 to the outermost observed star, while for the \mathcal{B} set, the computation stops at the angular radius
 809 corresponding to the tidal radius.

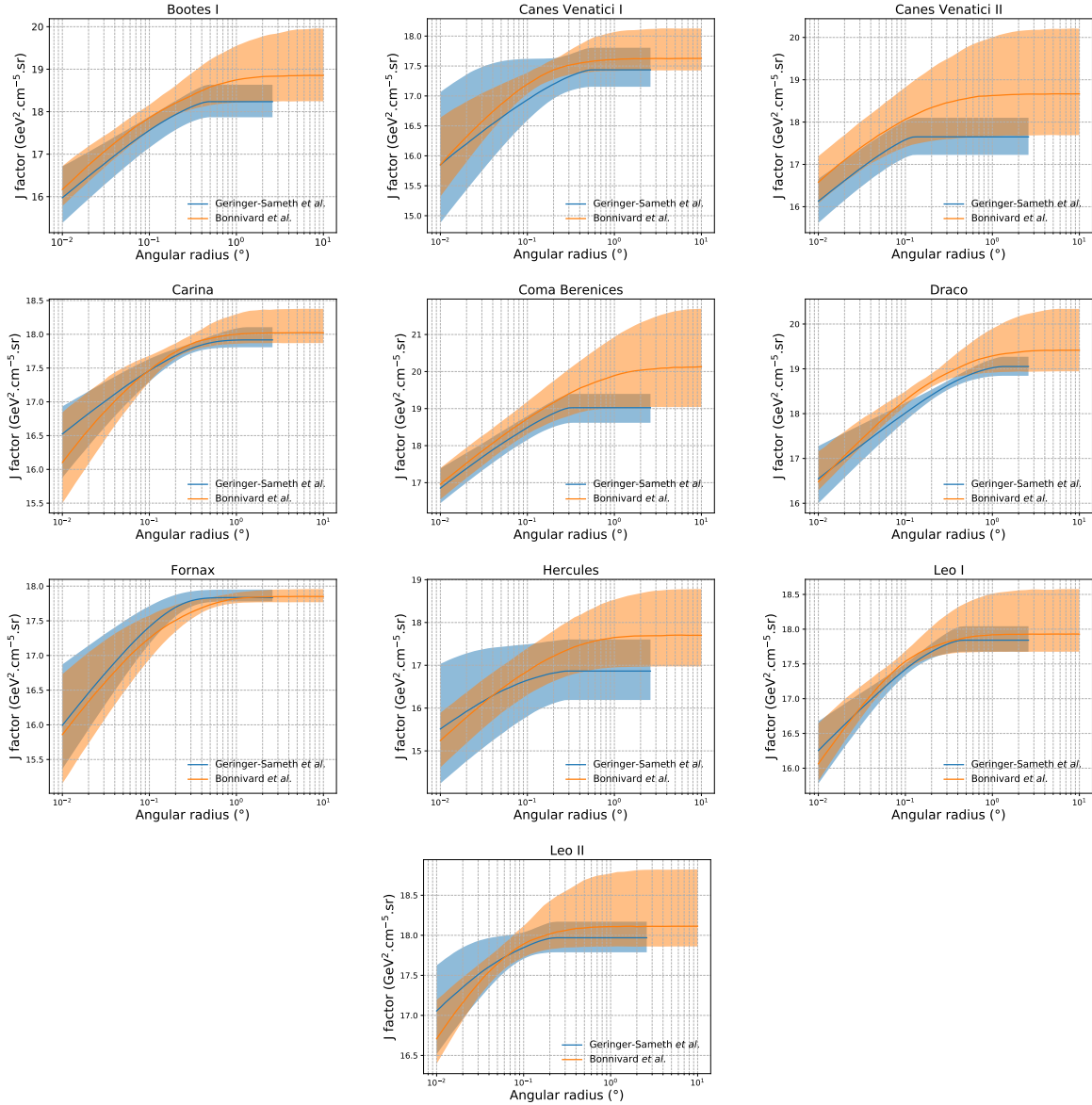


Figure 7.10 Comparisons between the J -factors versus the angular radius for the computation of J factors from Ref. [29] (\mathcal{GS} set in Table 7.1) in blue and for the computation from Ref. [31, 35] (\mathcal{B} set in Tab. 7.1) in orange. The solid lines represent the central value of the J -factors while the shaded regions correspond to the 1σ standard deviation.

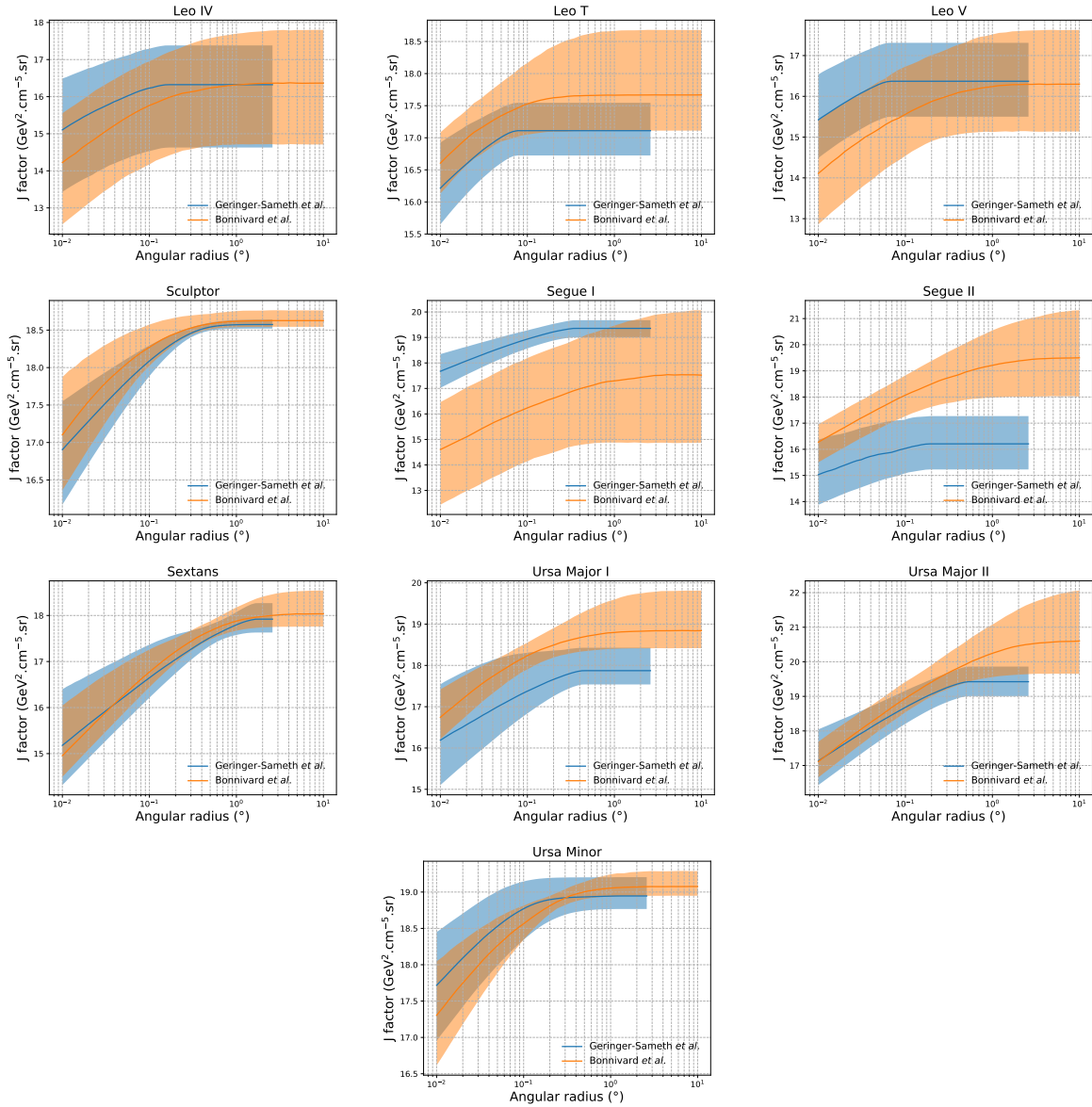


Figure 7.11 Comparisons between the J -factors versus the angular radius for the computation of J factors from Ref. [29] (\mathcal{GS} set in Tab. 7.1) in blue and for the computation from Ref. [31, 35] (\mathcal{B} set in Tab. 7.1) in orange. The solid lines represent the central value of the J -factors while the shaded regions correspond to the 1σ standard deviation.

810 7.7 Discussion and Conclusions

811 In this multi-instrument analysis, we have used observations of 20 dSphs from the gamma-ray
 812 telescopes Fermi-LAT, H.E.S.S., MAGIC, VERITAS, and HAWC to perform a collective DM
 813 search annihilation signals. The data were combined across sources and detectors to significantly
 814 increase the sensitivity of the search. We have observed no significant deviation from the null, no

815 DM, hypothesis, and so present our results in terms of upper limits on the annihilation cross section
816 for seven potential DM annihilation channels.

817 Fermi-LAT brings the most stringent constraints for continuum channels below approximately
818 1 TeV. the remaining detectors dominate at higher energies. Overall, for multi-TeV DM mass,
819 the combined DM constraints from all five telescopes are 2-3 times stronger than any individual
820 telescope for multi-TeV DM.

821 Derived from observations of many dSphs, our results produce robust limits given the DM
822 content of the dSphs is relatively well constrained. The obtained limits span the largest mass
823 range of any WIMP DM search. Our combined analysis improves the sensitivity over previously
824 published results from each detectors which produces the most stringent limits on DM annihilation
825 from dSphs. These results are based on deep exposures of the most promising known dSphs with
826 the currently most sensitive gamma-ray instruments. Therefore, our results constitute a legacy of
827 a generation of gamma-ray instruments on WIMP DM searches towards dSphs. Our results will
828 remain the reference in the field until a new generation of more sensitive gamma-ray instruments
829 begin operations, or until new dSphs with higher J -factors are discovered.

830 This analysis serves as a proof of concept for future multi-instrument and multi-messenger
831 combination analyses. With this collaborative effort, we have managed to sample over four orders
832 in magnitude in gamma-ray energies with distinct observational techniques. Determining the nature
833 of DM continues to be an elusive and difficult problem. Larger datasets with diverse measurement
834 techniques could be essential to tackling the DM problem. A future collaboration using similar
835 techniques as the ones described in this paper could grow even beyond gamma rays. The models we
836 used for this study include annihilation channels with neutrinos in the final state. Advanced studies
837 could aim to merge our results with those from neutrino observatories with large data sets. Efforts
838 are already underway to add data from the IceCube, ANTARES, and KM3NeT observatories to
839 these gamma-ray results.

840 From this work, a selection of the best candidates for observations, according to the latest
841 knowledge on stellar dynamics and modelling techniques for the derivation of the J -factors on the

842 potential dSphs targets, is highly desirable at the time that new experiments are starting their dark
843 matter programmes using dSphs. Given the systematic uncertainty inherent to the derivation of
844 the J -factors, an informed observational strategy would be to select both objects with the highest
845 J -factors that could lead to DM signal detection, and objects with robust J -factor predictions, i.e.
846 with kinematic measurements on many bright stars, which would strengthen the DM interpretation
847 reliability of the observation outcome.

848 This analysis combines data from multiple telescopes to produce strong constraints on astro-
849 physical objects. From this perspective, these methods can be applied beyond just DM searches.
850 Almost every astrophysical study can benefit from multi-telescope, multi-wavelength gamma-ray
851 studies. We have enabled these telescopes to study the cosmos with greater precision and detail.
852 Many astrophysical searches can benefit from multi-instrument gamma-ray studies, for which our
853 analysis lays the foundation.

CHAPTER 8

NU DUCK

854

BIBLIOGRAPHY

- 856 [1] Anne M. Green. “Dark matter in astrophysics/cosmology”. In: *SciPost Phys. Lect.*
 857 *Notes* (2022), p. 37. doi: [10.21468/SciPostPhysLectNotes.37](https://doi.org/10.21468/SciPostPhysLectNotes.37). URL: <https://scipost.org/10.21468/SciPostPhysLectNotes.37>.
- 859 [2] Bing-Lin Young. “A survey of dark matter and related topics in cosmology”. In: *Frontiers*
 860 *of Physics* 12 (Oct. 2016). doi: <https://doi.org/10.1007/s11467-016-0583-4>.
 861 URL: <https://doi.org/10.1007/s11467-016-0583-4>.
- 862 [3] Gianfranco Bertone, Dan Hooper, and Joseph Silk. “Particle dark matter: evidence,
 863 candidates and constraints”. In: *Physics Reports* 405.5 (2005), pp. 279–390. ISSN:
 864 0370-1573. doi: <https://doi.org/10.1016/j.physrep.2004.08.031>. URL:
 865 <https://www.sciencedirect.com/science/article/pii/S0370157304003515>.
- 866 [4] Gianfranco Bertone and Dan Hooper. “History of dark matter”. In: *Rev. Mod. Phys.*
 867 90 (4 Aug. 2018), p. 045002. doi: [10.1103/RevModPhys.90.045002](https://doi.org/10.1103/RevModPhys.90.045002). URL: <https://link.aps.org/doi/10.1103/RevModPhys.90.045002>.
- 869 [5] Fritz Zwicky. “The Redshift of Extragalactic Nebulae”. In: *Helvetica Physica Acta* 6.
 870 (1933), pp. 110–127. doi: [10.5169/seals-110267](https://doi.org/10.5169/seals-110267).
- 871 [6] Vera C. Rubin and Jr. Ford W. Kent. “Rotation of the Andromeda Nebula from a
 872 Spectroscopic Survey of Emission Regions”. In: *ApJ* 159 (Feb. 1970), p. 379. doi:
 873 [10.1086/150317](https://doi.org/10.1086/150317).
- 874 [7] K. G. Begeman, A. H. Broeils, and R. H. Sanders. “Extended rotation curves of spiral galaxies: dark haloes and modified dynamics”. In: *Monthly Notices of the Royal Astronomical Society* 249.3 (Apr. 1991), pp. 523–537. ISSN: 0035-8711. doi: [10.1093/mnras/249.3.523](https://doi.org/10.1093/mnras/249.3.523). eprint: <https://academic.oup.com/mnras/article-pdf/249/3/523/18160929/mnras249-0523.pdf>. URL: <https://doi.org/10.1093/mnras/249.3.523>.
- 879 [8] *Different types of gravitational lenses*. website. Feb. 2004. URL: <https://esahubble.org/images/heic0404b/>.
- 881 [9] Douglas Clowe et al. “A Direct Empirical Proof of the Existence of Dark Matter”. In: *apjl*
 882 648.2 (Sept. 2006), pp. L109–L113. doi: [10.1086/508162](https://doi.org/10.1086/508162). arXiv: [astro-ph/0608407](https://arxiv.org/abs/astro-ph/0608407)
 883 [[astro-ph](#)].
- 884 [10] Planck Collaboration and N. et. al. Aghanim. “Planck 2018 results I. Overview and the
 885 cosmological legacy of Planck”. In: *A&A* 641 (2020). doi: [10.1051/0004-6361/201833880](https://doi.org/10.1051/0004-6361/201833880). URL: <https://doi.org/10.1051/0004-6361/201833880>.
- 887 [11] Wayne Hu. *Matter Density Animation*. web. 2024. URL: <http://background.uchicago.edu/~whu/animbut/anim2.html>.

- 889 [12] Wenlong Yuan et al. “A First Look at Cepheids in a Type Ia Supernova Host with JWST”. in:
890 *The Astrophysical Journal Letters* 940.1 (Nov. 2022). doi: [10.3847/2041-8213/ac9b27](https://doi.org/10.3847/2041-8213/ac9b27).
891 URL: <https://dx.doi.org/10.3847/2041-8213/ac9b27>.
- 892 [13] Wendy L. Freedman. “Measurements of the Hubble Constant: Tensions in Perspective”. In:
893 *The Astrophysical Journal* 919.1 (Sept. 2021), p. 16. doi: [10.3847/1538-4357/ac0e95](https://doi.org/10.3847/1538-4357/ac0e95).
894 URL: <https://dx.doi.org/10.3847/1538-4357/ac0e95>.
- 895 [14] Jodi Cooley. “Dark Matter direct detection of classical WIMPs”. In: *SciPost Phys. Lect.
896 Notes* (2022), p. 55. doi: [10.21468/SciPostPhysLectNotes.55](https://doi.org/10.21468/SciPostPhysLectNotes.55). URL: <https://scipost.org/10.21468/SciPostPhysLectNotes.55>.
- 897 [15] “Search for new phenomena in events with an energetic jet and missing transverse momentum
898 in pp collisions at $\sqrt{s} = 13$ TeV with the ATLAS detector”. In: *Phys. Rev. D* 103
900 (11 July 2021), p. 112006. doi: [10.1103/PhysRevD.103.112006](https://doi.org/10.1103/PhysRevD.103.112006). URL: <https://link.aps.org/doi/10.1103/PhysRevD.103.112006>.
- 901 [16] *Jetting into the dark side: a precision search for dark matter*. website. July 2020. URL:
902 <https://atlas.cern/updates/briefing/precision-search-dark-matter>.
- 903 [17] Celine Armand et. al. “Combined dark matter searches towards dwarf spheroidal galaxies
904 with Fermi-LAT, HAWC, H.E.S.S., MAGIC, and VERITAS”. in: *Proceedings of Science*.
905 Vol. 395. Mar. 2022. doi: <https://doi.org/10.22323/1.395.0528>.
- 906 [18] Tracy R. Slatyer. “Les Houches Lectures on Indirect Detection of Dark Matter”. In: *SciPost
907 Phys. Lect. Notes* (2022), p. 53. doi: [10.21468/SciPostPhysLectNotes.53](https://doi.org/10.21468/SciPostPhysLectNotes.53). URL:
908 <https://scipost.org/10.21468/SciPostPhysLectNotes.53>.
- 909 [19] Christian W Bauer, Nicholas L. Rodd, and Bryan R. Webber. “Dark matter spectra from
910 the electroweak to the Planck scale”. In: *Journal of High Energy Physics* 2021.1029-8479
911 (June 2021). doi: [https://doi.org/10.1007/JHEP06\(2021\)121](https://doi.org/10.1007/JHEP06(2021)121).
- 912 [20] Riccardo Catena and Piero Ullio. “A novel determination of the local dark matter density”.
913 In: *Journal of Cosmology and Astroparticle Physics* 2010.08 (Aug. 2010), p. 004. doi:
914 [10.1088/1475-7516/2010/08/004](https://doi.org/10.1088/1475-7516/2010/08/004). URL: <https://dx.doi.org/10.1088/1475-7516/2010/08/004>.
- 915 [21] B. P. Abbott et al. “Observation of Gravitational Waves from a Binary Black Hole Merger”.
916 In: *Phys. Rev. Lett.* 116 (6 Feb. 2016), p. 061102. doi: [10.1103/PhysRevLett.116.061102](https://doi.org/10.1103/PhysRevLett.116.061102). URL: <https://link.aps.org/doi/10.1103/PhysRevLett.116.061102>.
- 917 [22] R. Abbasi et. al. “Observation of high-energy neutrinos from the Galactic plane”. In: *Science*
918 380.6652 (June 2023), pp. 1338–1343.
- 919 [23] NASA Goddard Space Flight Center. *Fermi’s 12-year view of the gamma-ray sky*. website.

- 923 2022. URL: <https://svs.gsfc.nasa.gov/14090>.
- 924 [24] Marco Cirelli et al. “PPPC 4 DM ID: a poor particle physicist cookbook for dark matter
925 indirect detection”. In: *Journal of Cosmology and Astroparticle Physics* 2011.03 (Mar.
926 2011), p. 051. doi: [10.1088/1475-7516/2011/03/051](https://doi.org/10.1088/1475-7516/2011/03/051). URL: <https://dx.doi.org/10.1088/1475-7516/2011/03/051>.
- 928 [25] A. U. Abeysekara et al. “Observation of the Crab Nebula with the HAWC Gamma-Ray
929 Observatory”. In: *The Astrophysical Journal* 843.1 (June 2017), p. 39. doi: [10.3847/1538-4357/aa7555](https://doi.org/10.3847/1538-4357/aa7555). URL: <https://doi.org/10.3847/1538-4357/aa7555>.
- 931 [26] A. Albert et al. “Dark Matter Limits from Dwarf Spheroidal Galaxies with the HAWC
932 Gamma-Ray Observatory”. In: *The Astrophysical Journal* 853.2 (Feb. 2018), p. 154. ISSN:
933 1538-4357. doi: [10.3847/1538-4357/aaa6d8](https://doi.org/10.3847/1538-4357/aaa6d8). URL: <http://dx.doi.org/10.3847/1538-4357/aaa6d8>.
- 935 [27] Giacomo Vianello et al. *The Multi-Mission Maximum Likelihood framework (3ML)*. 2015.
936 arXiv: [1507.08343](https://arxiv.org/abs/1507.08343) [astro-ph.HE].
- 937 [28] Marco Cirelli et al. “PPPC 4 DM ID: a poor particle physicist cookbook for dark matter
938 indirect detection”. In: *Journal of Cosmology and Astroparticle Physics* 2011.03 (Mar.
939 2011). ISSN: 1475-7516. doi: [10.1088/1475-7516/2011/03/051](https://doi.org/10.1088/1475-7516/2011/03/051). URL: <http://dx.doi.org/10.1088/1475-7516/2011/03/051>.
- 941 [29] Alex Geringer-Sameth and Matthew Koushiappas Savvas M. and Walker. “Dwarf galaxy
942 annihilation and decay emission profiles for dark matter experiments”. In: *Astrophys.
943 J.* 801.2 (2015), p. 74. doi: [10.1088/0004-637X/801/2/74](https://doi.org/10.1088/0004-637X/801/2/74). arXiv: [1408.0002](https://arxiv.org/abs/1408.0002)
944 [astro-ph.CO].
- 945 [30] Alex Geringer-Sameth, Savvas M. Koushiappas, and Matthew Walker. “DWARF GALAXY
946 ANNIHILATION AND DECAY EMISSION PROFILES FOR DARK MATTER EXPERI-
947 MENTS”. in: *The Astrophysical Journal* 801.2 (Mar. 2015), p. 74. ISSN: 1538-4357. doi:
948 [10.1088/0004-637x/801/2/74](https://doi.org/10.1088/0004-637x/801/2/74). URL: <http://dx.doi.org/10.1088/0004-637X/801/2/74>.
- 950 [31] V. Bonnivard et al. “Spherical Jeans analysis for dark matter indirect detection in dwarf
951 spheroidal galaxies - Impact of physical parameters and triaxiality”. In: *Mon. Not. Roy.
952 Astron. Soc.* 446 (2015), pp. 3002–3021. doi: [10.1093/mnras/stu2296](https://doi.org/10.1093/mnras/stu2296). arXiv:
953 [1407.7822](https://arxiv.org/abs/1407.7822) [astro-ph.HE].
- 954 [32] M. Ackermann et al. “Searching for Dark Matter Annihilation from Milky Way Dwarf
955 Spheroidal Galaxies with Six Years of Fermi Large Area Telescope Data”. In: *prl* 115.23,
956 231301 (Dec. 2015), p. 231301. doi: [10.1103/PhysRevLett.115.231301](https://doi.org/10.1103/PhysRevLett.115.231301). arXiv:
957 [1503.02641](https://arxiv.org/abs/1503.02641) [astro-ph.HE].

- 958 [33] A. et al. Albert. “Searching for Dark Matter Annihilation in Recently Discovered Milky Way
 959 Satellites with Fermi-LAT”. In: *Astrophys. J.* 834.2 (2017), p. 110. doi: [10.3847/1538-4357/834/2/110](https://doi.org/10.3847/1538-4357/834/2/110). arXiv: [1611.03184](https://arxiv.org/abs/1611.03184) [astro-ph.HE].
- 961 [34] Mattia Di Mauro and Martin Wolfgang Winkler. “Multimessenger constraints on the dark
 962 matter interpretation of the Fermi-LAT Galactic Center excess”. In: *prd* 103.12, 123005
 963 (June 2021), p. 123005. doi: [10.1103/PhysRevD.103.123005](https://doi.org/10.1103/PhysRevD.103.123005). arXiv: [2101.11027](https://arxiv.org/abs/2101.11027)
 964 [astro-ph.HE].
- 965 [35] V. Bonnivard et al. “Dark matter annihilation and decay in dwarf spheroidal galaxies: The
 966 classical and ultrafaint dSphs”. In: *Mon. Not. Roy. Astron. Soc.* 453.1 (2015), pp. 849–867.
 967 doi: [10.1093/mnras/stv1601](https://doi.org/10.1093/mnras/stv1601). arXiv: [1504.02048](https://arxiv.org/abs/1504.02048) [astro-ph.HE].
- 968 [36] Gianfranco Bertone, Dan Hooper, and Joseph Silk. “Particle dark matter: evidence, can-
 969 didates and constraints”. In: *Physics Reports* 405.5-6 (Jan. 2005), pp. 279–390. ISSN:
 970 0370-1573. doi: [10.1016/j.physrep.2004.08.031](https://doi.org/10.1016/j.physrep.2004.08.031). URL: <http://dx.doi.org/10.1016/j.physrep.2004.08.031>.
- 972 [37] HongSheng Zhao. “Analytical models for galactic nuclei”. In: *Mon. Not. Roy. Astron. Soc.*
 973 278 (1996), pp. 488–496. doi: [10.1093/mnras/278.2.488](https://doi.org/10.1093/mnras/278.2.488). arXiv: [astro-ph/9509122](https://arxiv.org/abs/astro-ph/9509122)
 974 [astro-ph].
- 975 [38] H. C. Plummer. “On the Problem of Distribution in Globular Star Clusters: (Plate 8.)”
 976 In: *Monthly Notices of the Royal Astronomical Society* 71.5 (Mar. 1911), pp. 460–470.
 977 ISSN: 0035-8711. doi: [10.1093/mnras/71.5.460](https://doi.org/10.1093/mnras/71.5.460). eprint: <https://academic.oup.com/mnras/article-pdf/71/5/460/2937497/mnras71-0460.pdf>. URL:
 979 <https://doi.org/10.1093/mnras/71.5.460>.
- 980 [39] Daniel R. Hunter. “Derivation of the anisotropy profile, constraints on the local velocity
 981 dispersion, and implications for direct detection”. In: *JCAP* 02 (2014), p. 023. doi:
 982 [10.1088/1475-7516/2014/02/023](https://doi.org/10.1088/1475-7516/2014/02/023). arXiv: [1311.0256](https://arxiv.org/abs/1311.0256) [astro-ph.CO].
- 983 [40] Barun Kumar Dhar and Liliya L. R. Williams. “Surface mass density of the Einasto family
 984 of dark matter haloes: are they Sersic-like?” In: *Mon. Not. Roy. Astron. Soc.* (2010). doi:
 985 [10.1111/j.1365-2966.2010.16446.x](https://doi.org/10.1111/j.1365-2966.2010.16446.x).
- 986 [41] M. Baes and E. Van Hese. “Dynamical models with a general anisotropy profile”. In: *Astron. Astrophys.* 471 (2007), p. 419. doi: [10.1051/0004-6361:20077672](https://doi.org/10.1051/0004-6361:20077672). arXiv: [0705.4109](https://arxiv.org/abs/0705.4109) [astro-ph].
- 989 [42] Matthew G. Walker, Edward W. Olszewski, and Mario Mateo. “Bayesian analysis of re-
 990 solved stellar spectra: application to MMT/Hectochelle observations of the Draco dwarf
 991 spheroidal”. In: *mnras* 448.3 (Apr. 2015), pp. 2717–2732. doi: [10.1093/mnras/stv099](https://doi.org/10.1093/mnras/stv099).
 992 arXiv: [1503.02589](https://arxiv.org/abs/1503.02589) [astro-ph.GA].